

89N19232

NASA  
Technical  
Paper  
**2895**

C.3

April 1989

Drag Measurements on  
a Laminar-Flow Body of  
Revolution in the 13-Inch  
Magnetic Suspension and  
Balance System

David A. Dress

TECHNICAL REPORTS  
FILE COPY

PROPERTY OF U.S. AIR FORCE  
AEDC TECHNICAL LIBRARY

NASA

**NASA  
Technical  
Paper  
2895**

1989

**Drag Measurements on  
a Laminar-Flow Body of  
Revolution in the 13-Inch  
Magnetic Suspension and  
Balance System**

David A. Dress  
*Langley Research Center*  
*Hampton, Virginia*



National Aeronautics and  
Space Administration  
Office of Management  
Scientific and Technical  
Information Division

## Abstract

Wind tunnel measurements of drag force at low speeds were taken for a laminar-flow body of revolution free of support interference. This body was tested at zero incidence in the 13-inch Magnetic Suspension and Balance System (MSBS) at the Langley Research Center. The primary objective of these tests was to substantiate the capabilities of the MSBS for measuring drag force. The drag-force calibrations and wind-on repeatability data provided the means of assessing these capabilities. Additional investigations included (1) the effects of fixing transition, (2) the effects of fins installed in the tail, and (3) surface flow visualizations using both liquid crystals and oil flow. Two simple drag prediction codes were used to assess their usefulness in estimating overall body drag. These theoretical results did not compare well with the measured values because of incorrect or nonexistent modeling of a laminar separation bubble on the body.

## Introduction

Support interference is a serious problem when testing models in wind tunnels (refs. 1 and 2). Figure 1 shows three examples of model support interference problems. In each case, the sting support required a model geometry different from the aircraft geometry. The presence of the sting also distorted the base flow in each case. This combination of geometry modification and distorted base flow produced the errors shown. Using a magnetic suspension and balance system (MSBS) is the only way to eliminate support interference completely. With the elimination of the support, not only will the flow distortion produced by the sting be eliminated, but also many other advantages will accrue, such as

1. elimination of model modifications to accommodate the sting
2. ease of model movement for dynamic testing
3. fast, efficient testing at any attitude
4. improvement in productivity by elimination of stings and struts

Other potential advantages are presented in reference 3.

An MSBS is a device capable of both suspending a model in space and measuring the forces and moments acting upon it. These actions are accomplished through the use of controlled magnetic fields interacting with a magnetized core placed in the model. In a wind tunnel, an MSBS uses electromagnets positioned external to the test section. The core is either a permanent magnet, magnetized soft iron, or a solenoid within the model. The position of the

suspended model is inherently unstable, and a closed-loop feedback control system which incorporates a method of sensing the model position and attitude is therefore required to stabilize the model by actively controlling the applied magnetic fields (refs. 4 and 5). The MSBS can counteract a range of external forces and moments applied to the model while maintaining the model at any arbitrary position. The amount of electrical current flowing in each of the external electromagnets is used to determine the forces and moments acting on the suspended model.

The French at ONERA first demonstrated a wind tunnel MSBS in the mid-1950's (ref. 6). Since that time, considerable research has been devoted to MSBS's and many improvements have been made (ref. 7). Today, applying MSBS's to routine wind tunnel testing of aircraft models is practical; however, they are still not widely used. This is principally because of the small size of all existing systems.

Recent technical advances have removed some of the barriers to building large MSBS's. One example is progress with large superconducting electromagnets which would be needed to support the weight of the model and also to counteract the large aerodynamic loads. Another advance is the use of a superconducting solenoid as a model core (ref. 8) to produce a model with the highest possible magnetic moment. Using this type of core would reduce the overall system cost by minimizing the required size of the external electromagnets. In addition to these advances, feasibility and conceptual design studies (refs. 9 to 11) have produced innovative MSBS designs. These new designs significantly reduce the cost of large systems, making them more affordable for large wind tunnels. Additional developments are needed in a few hardware technologies in order to fully use a large MSBS. These technologies include (1) very-high-capacity, energy-efficient power amplifiers and (2) wide-ranging, accurate, and versatile model position sensors. It is anticipated that work in these and related branches of engineering will result in steady development.

Since the late 1970's, in-house activity with MSBS's has steadily increased at NASA Langley Research Center. In 1979 the U.S. Air Force loaned the 13-in. MSBS at the Arnold Engineering Development Center (AEDC, ref. 12) to researchers at Langley. The system was initially used to gain operational experience with a working MSBS. Ownership of the system has since transferred to NASA from the Air Force.

Early in 1984 this 13-in. MSBS was combined with a small, low-speed ( $M \leq 0.5$ ) wind tunnel. The primary goal was to gain some practical experience with this system, with the emphasis placed on using

and understanding the MSBS rather than on obtaining aerodynamic data. The 13-in. MSBS was then modified in several respects. The original AEDC X-ray position sensors were replaced with an electro-optical system which uses solid-state linear photodiode arrays, and the original analog control system was replaced with a digital controller which uses a minicomputer (ref. 13). These and other improvements make the system easier to use.

However, several limitations still exist with the 13-in. MSBS. One is a limit on available angles-of-attack ( $\pm 5^\circ$ ). Another is difficulty in suspending irregular-shaped three-dimensional models. Both of these limitations arise because of the design and nature of the electro-optical position sensing system. Despite these limitations, the emphasis at the present time is on using the 13-in. MSBS to obtain useful aerodynamic data. The existing position sensing system works well with most axisymmetric shapes. Therefore, a program is underway to obtain accurate drag data on various axisymmetric shapes at zero incidence.

As part of this program, wind tunnel measurements of drag force at low speeds were taken on a laminar-flow body of revolution free of support interference in the Langley 13-in. MSBS. The primary objective of these tests was to substantiate the drag-force measuring capabilities of the MSBS. Generally, a multicomponent strain-gage balance is accurate to  $\pm 0.5$  percent of full scale. The basic accuracy of a multicomponent magnetic balance should equal or exceed that of a standard multicomponent strain-gage balance; however, the obvious advantage of an MSBS is the total elimination of support interference. In this context, aerodynamic data from an MSBS is more accurate than data obtained from a conventionally supported model with a strain-gage balance. The axisymmetric body used in this study was chosen because the unique data set produced would be of interest to researchers involved in designing minimum-drag fuselages.

## Symbols

<i>A</i>	polynomial coefficient from drag-force calibration equation	
<i>A</i> <sub>max</sub>	maximum cross-sectional area of model, in <sup>2</sup>	
<i>b</i>	tunnel width, in.	
<i>B</i>	polynomial coefficient from drag-force calibration equation	
<i>C</i>	polynomial coefficient from drag-force calibration equation	
		Subscripts:
		<i>B</i>
		<i>b</i>
		<i>c</i>
		<i>cv</i>
		<i>L</i>
		<i>0</i>
		due to buoyancy
		due to blockage
		corrected value
		measured in the cavity at the rear of the model
		based on model length
		based on zero axial load

<i>s</i>	static condition
<i>s'</i>	due to solid blockage
<i>t</i>	total condition
<i>w</i>	due to wake blockage
wet	based on wetted surface area
wo	wind on
woff	wind off

## Description of 13-in. MSBS

Figure 2(a) shows a sketch of the arrangement of the 13-in. MSBS which was originally constructed at the U.S. Air Force AEDC in the early 1960's. For this system, motion is controlled in 5 degrees of freedom with no provision for generation of controlled magnetic roll torque on the model. Figure 2(b) shows a photograph of the system. This system has four electromagnets, arranged in a V-configuration above the wind tunnel test section, that provide the lift force, pitching moment, side force, and yawing moment. The 13-in. MSBS has a lift force capability of about 6 lbf depending on the size and shape of the iron core in the model. The drag electromagnet counteracts the drag force. The test section for the tunnel passes through the drag electromagnet.

All the electromagnets have conventional copper windings. The drag electromagnet is fed from a bipolar thyristor power supply, while the other electromagnets are fed from a mix of unipolar thyratron supplies and rectified motor-driven variable transformers. The bipolar supply used with the drag electromagnet enables it to both push and pull on the model. Note that each of the four main electromagnets is composed of two sets of windings per pole, a set of bias windings and a set of control windings. The bias windings supply a steady current necessary to suspend a model. This reduces the amount of control current needed during actual operation.

The control system is completely digitized, with a minicomputer handling all the control functions (ref. 13). Typical feedback loop repetition rates for this system are on the order of 256 cycles per second. The 13-in. MSBS uses an optical position sensing system based on solid-state linear photodiode arrays. Laser light sheets are directed across the test section to illuminate the arrays. The model position and attitude are inferred by locating the shadow of the model on the arrays. This technique is very dependent on geometry. Abrupt changes in shadow positions are generally not tolerated by the control system; therefore, it is difficult to suspend many non-axisymmetric shapes, especially bodies with wings at

various pitch or yaw angles. Reference 14 gives more details on this optical position sensing system.

Figures 3, 4, and 5 are photographs of the laminar-flow body suspended in the 13-in. MSBS. Figure 3 is a view of the 13-in. MSBS from the control room. Figure 4 is a close-up of the suspended laminar-flow body, and figure 5 is a view from the contraction section of the tunnel looking at the nose of the suspended body.

## Description of Wind Tunnel

A small, low-speed ( $M \leq 0.5$ ) wind tunnel was adapted to use with the 13-in. MSBS. As shown in figure 6, the tunnel is an open-circuit design with air drawn into the tunnel from outside the building through a large bellmouth protected from outside contaminants by a screen enclosure. Constant-diameter ducting extends the circuit to the first turn. Following the first turn, a quick (rapid area) diffuser and settling chamber with screens and honeycomb prepare the flow for entry into the contraction and test sections. The contraction ratio is 8.43.

The clear General Electric Lexan thermoplastic test section is a modified octagon shape with major and minor axes of 12.56 and 10.69 in., respectively. (See fig. 7.) At the end of the diffuser, a section of 2.5-in.-thick honeycomb is used to protect the fan. A turn identical to the inlet turn directs the flow to the fan section and then to the exit outside the building. A water-cooled, 200-hp, 6000-rpm, variable frequency electric motor drives the fan. Reference 15 gives full details on the tunnel layout and calibration.

The flow quality in the tunnel is as follows

1. a maximum deviation of  $\pm 0.25$  percent in dynamic pressure across the test section
2. velocity fluctuations in the streamwise direction of 0.2 percent  $\pm 0.1$  percent for the Reynolds number range of  $2 \times 10^5 \text{ ft}^{-1}$  to  $2 \times 10^6 \text{ ft}^{-1}$
3. flow angularity in pitch of about  $-0.5^\circ$  relative to the cathetometer reference (see *Test Procedure* section)

## Description of Model

Figure 8 shows a photograph of the model used in this study which has a long favorable pressure gradient forebody. The body profile was generated from an eight-parameter class of rounded-nose, tail-boom bodies described in reference 16. This class of bodies was developed to verify a method of shaping axisymmetric bodies to produce minimum drag in incompressible, nonseparating flow at zero incidence. An optimization scheme constrained to exclude turbulent separation is used to minimize  $C_D$ . This scheme,

which achieves drag reduction by body-shape modification, results in bodies with extended runs of laminar flow.

A sting-mounted version of this shape was previously tested in a towing tank at the United States Naval Academy (refs. 17 and 18). The model tested by the Navy was slightly modified from the design shape in the tail region in order to accommodate the sting. (See fig. 9.) One of the goals of these tests was to quantify the hydrodynamic performance of this body. Additional computational results on this body are found in references 19 and 20.

The model used for the present study was 12 in. long with a maximum diameter of 2.67 in. The model, which weighed about 2 lb, was made in two longitudinal halves with a fiberglass skin that was foam filled around an embedded soft iron core. This ultralow-carbon iron core was magnetized by the applied magnetic fields. The core was 1 in. in diameter by 6 in. long and it was centered in the model. Because of the lack of roll control for the 13-in. MSBS, the model was weighted to provide a constant roll position. This was done during fabrication by placing a 20-g brass weight against the inside surface of the model's skin.

The eight nondimensional parameters listed below were used to generate this body of revolution according to the method described in reference 16.

$$\begin{array}{ll} r_n = 0.50 & x_i = 0.80 \\ f_n = 4.5 & r_i = 0.50 \\ x_m = 0.5555 & s_i = 2.0 \\ k_i = 1.50 & t = 0.3 \end{array}$$

The symbols used are defined in reference 16. Table I lists the coordinates of the model.

## Description of Surface Flow Visualization Techniques

### Liquid Crystals

A liquid crystal surface flow visualization technique was used to determine transition and separation locations. This technique is discussed in detail in references 21 to 23. Liquid crystals have properties of both liquid-phase and solid-phase materials. They can display the optical properties of solid crystals by scattering light very selectively. These optical characteristics can be displayed by altering the molecular structure of the liquid crystals. The molecular structure is primarily influenced by temperature and shear stress, which cause the liquid crystals to selectively reflect various colors.

Liquid crystals with a wide temperature bandwidth were chosen for this study so that shear stress would dominate in determining the liquid crystal color response. This shear stress response can be used to visualize various boundary layer flows, including transition and separation. Liquid crystals indicate transition by changing colors in response to the large shear stress change through the transitional region. (See fig. 10, taken from ref. 23.) Separation is indicated by a change from "color" to "no color" at a point on a body because  $C_f$  is zero in a separated region.

For the present study, the models were painted flat black. As noted in reference 23, this provides the best background surface for visualizing liquid crystals. The liquid crystals were thinned with a solvent and applied by spraying a thin coat on the model surface. A good application results in a coating thickness of approximately 0.0005 to 0.0010 in. One coat could be used for several tunnel runs at different Reynolds numbers.

### Pigmented Oil

A pigmented oil surface flow visualization technique was also used to determine separation locations. This is a type of oil flow which uses a mixture of titanium dioxide ( $TiO_2$ ) suspended in refined mineral oil. A small amount of oleic acid is added as an anticoagulant. After the mixture was brushed on the black model surface, the model was placed in the tunnel and suspended. The tunnel was then brought to test conditions, and after the excess oil was wiped off, the  $TiO_2$  was left deposited on the surface.

## Description of Drag Prediction Codes

### SANDRAG Code

A simple and efficient drag prediction code, SANDRAG, was used to obtain a theoretical estimate of  $C_{D,wet}$  for this body (refs. 24 and 25). SANDRAG calculates the flow field and drag of bodies of revolution at zero incidence in incompressible flow by using a combination of a potential-flow method and boundary-layer techniques. This code has been used successfully to predict drag for some simple axisymmetric projectile shapes. The goal for this study was to verify the usefulness of this code in predicting drag for the more complicated axisymmetric shape used. An axial distribution of source and sink elements is used to form the body for the potential solution, with the equations applying to both open and closed bodies. The body used for this study is considered an open body because the surface does

not return to the axis at the tail. The laminar- and turbulent-boundary-layer solutions use momentum integral techniques which account for the effects of surface roughness. Transition is modeled by taking into account the effects of pressure gradient and surface roughness. Separation is also modeled by predicting separation locations and estimating the drag based on the pressure in the separated region (separation drag). In the laminar boundary layer, separation is based only on the pressure gradient, while in the turbulent boundary layer, separation is based on the value of the shape factor. Finally, the base pressure coefficient is estimated with data correlations from various afterbody shapes.

### Nakayama and Patel Code

A simple code was developed by Nakayama and Patel to calculate the viscous resistance, or skin-friction drag, of a streamlined body of revolution at zero incidence in incompressible flow (ref. 26). This code calculates the flow field and drag by using a combination of a potential-flow method and momentum-integral boundary-layer techniques. The Nakayama and Patel code has been used to calculate fairly accurate drag coefficients for simple airship shapes in cases where the transition point is known or is predicted accurately (ref. 26). Once again, the goal in this study was to verify the usefulness of this code in predicting drag for the more complicated axisymmetric shape used.

Several empirical correlations are used to predict transition. In addition, the experimental transition location can be used. This code was primarily developed to evaluate the flow in the tail region. The turbulent-boundary-layer calculations are made with Patel's integral method (ref. 27), which accounts for thick turbulent boundary layers. Separation is not modeled by this code; in addition, this code does not provide estimates of base pressure drag.

### Test Procedure

For this study, the model was tested at zero incidence. The pitch attitude, vertical position, and horizontal position of the model were verified with an optical cathetometer. This is a remote fixed device used to measure relative vertical and horizontal displacements. (See fig. 11.) The pitch attitude, vertical position, and horizontal position were accurate to approximately  $\pm 0.02^\circ$ ,  $\pm 0.002$  in., and  $\pm 0.002$  in., respectively. The model pitch attitude was not corrected for the flow angularity mentioned earlier. The yaw attitude and lateral model position relative to the test section sidewall were verified by shining a laser light sheet longitudinally across the top of the

model. It is estimated that the yaw attitude and lateral position were accurate to  $\pm 0.6^\circ$  and  $\pm 0.1$  in., respectively.

The initial phase of testing consisted of a drag-force calibration. The calibration involved suspending the model with no wind and loading it in the axial direction. For this type of calibration the electromagnets above the test section suspend the model by supporting its weight. The drag electromagnet works to counteract the applied load. The loading was performed with the traditional string, pulley, and weight pan combination shown in figure 12.

A data acquisition unit (DAU) and a microcomputer were used to read and record the data. (See fig. 13.) The DAU was interfaced directly with the shunts which provide a means of measuring the current in the electromagnets. For a given weight or load, shunt voltages and magnet currents were recorded with the microcomputer. Voltages were converted on-line to obtain equivalent currents using a calibration of shunt voltage versus current performed prior to these tests. The computer software continuously updated and displayed the last five values and the average values of both shunt voltages and magnet currents on the screen. These values were also recorded as the model was unloaded to check for hysteresis. The drag electromagnet current was plotted against the load to determine a calibration curve for the model.

To record wind-on drag measurements, the model was suspended at the same location where the calibration was performed. For a given Mach number, shunt voltages and magnet currents as well as tunnel conditions ( $p_s$ ,  $p_t$ , and  $T_t$ ) were recorded with the DAU and the microcomputer. A typical data point contains the last five readings of the voltages, currents, and tunnel parameters.

The drag force was obtained directly from the drag electromagnet current through the use of the calibration curve fit shown in figure 14. Buoyancy corrections were applied to this drag-force data. These corrections were rather large, primarily because of the low drag forces present on the laminar-flow body. The drag coefficients corrected for buoyancy were reduced by 7 to 14 percent, depending on the tunnel speed.

Both solid and wake blockage corrections were also applied to the results of this study. The drag coefficients corrected for blockage were reduced by 5 percent. Further details on the data reduction and corrections are in the appendix.

## Discussion of Experimental Results

### Drag-Force Calibration

As mentioned previously, the calibration was performed with the setup shown in figure 12. Electromagnet current measurements were recorded as the model was loaded from 5 to 242.5 gf. Current measurements were also recorded as the model was unloaded to check for hysteresis. The results from this calibration, shown in figure 14, indicate that there is no significant hysteresis in these data. The data were fitted with a second-order polynomial. Figure 15 shows an error plot for this drag-force calibration. These errors are the differences between the applied loads and the calculated loads from the polynomial equation. The root-mean-square (rms) value for these errors is 0.27 gf, or 0.11 percent of the full-scale calibration load of 242.5 gf.

The small uncertainty of  $\pm 0.11$  percent in this calibration may be attributable to a small amount of magnetic hysteresis present in the model core. Another possible cause is intermittent vibrations of the model due to slight vibrations of the optical position sensing system. Prior to these tests, a study was performed in the 13-in. MSBS comparing the effects of core material on calibration results. Two different core materials were used, mild steel and the same ultralow-carbon iron used with the present study. The ultralow-carbon iron exhibited much less magnetic hysteresis than the mild steel.

Following the wind-on data runs for the laminar-flow body, an additional drag-force calibration was performed with the same loading range repeated. Figure 16 shows the results of this calibration compared with the results of the first calibration from figure 14. This second calibration was also fitted with a second-order polynomial. The two curve fits are slightly displaced, with a maximum shift of 0.92 percent. These differences can be attributed to the following two factors:

1. Inaccuracies were present in positioning the model at the same location for both calibrations; the inaccuracies existed primarily in the yaw attitude and lateral position. Recall that the yaw attitude and lateral position were accurate to  $\pm 0.6^\circ$  and  $\pm 0.1$  in., respectively.
2. Inaccuracies were present in the pitch angle of the calibration line used to pull on the model. This angle, which was also measured by the cathetometer, was approximately  $\pm 0.75^\circ$  from  $0^\circ$  in pitch.

### Drag-Force Characteristics and Repeatability of Data

Wind-on drag-force measurements were taken for this body at Mach numbers from approximately 0.05 to 0.20. The results, presented in figure 17, indicate that  $C_{D,\text{wet}}$  decreases as  $R_L$  increases. Also shown in figure 17 is a repeat run for comparison; there is excellent repeatability of the data. The rms of the differences in drag force between the first and second runs is approximately 1.4 gf, or 0.58 percent of the maximum calibration load of 242.5 gf. The differences are larger at the higher Mach numbers because of vibrations exhibited by the model at these speeds as a result of static aerodynamic stability problems. Table II lists both the corrected and uncorrected drag coefficients for run 1.

In reference 28, Hoerner shows the general trends of drag coefficient versus Reynolds number for streamlined bodies of revolution. (See fig. 22 in chapter VI of ref. 28.) In the Reynolds number region from  $10^4$  to  $10^5$ , Hoerner has estimated the drag coefficient assuming there is laminar boundary-layer separation without reattachment, as in the case of flow over a spheroid. From  $R = 10^5$  to  $10^6$ ,  $C_{D,\text{wet}}$  decreases drastically because of the onset of transition and turbulent flow. The turbulent flow energizes the boundary layer and carries the flow farther around the body, the result being a smaller wake and thus a lower drag coefficient than is present with laminar separation. From  $R = 10^5$  to around  $10^7$ , transition is moving forward. At around  $R = 10^7$ , there is fully turbulent flow over the bodies. The data from the present study follow some of the same trends as those shown in the figure in reference 28. In particular, the data from this study follow a nearly constant slope for Reynolds numbers from  $4 \times 10^5$  to  $8 \times 10^5$ . This trend is very similar to the data trend shown by Hoerner for Reynolds numbers from  $10^4$  to  $10^5$ . Also, the data from this study drop off drastically for Reynolds numbers from  $8.0 \times 10^5$  to  $1.3 \times 10^6$ . This trend is very similar to the data trend shown by Hoerner for Reynolds numbers from  $10^5$  to  $10^6$ .

Figure 18 is an oil flow photograph from the present study showing a laminar separation bubble at  $R_L = 1.2 \times 10^6$ . Figure 19 is a liquid crystal flow visualization photograph also showing this laminar separation region at the same  $R_L$ . A laminar separation line and turbulent reattachment line are shown in both figures. At lower values of  $R_L$  it was observed that the separation line was at a more forward station on the body. It is estimated that this separation line originated between  $x/L = 0.50$  and  $x/L = 0.55$ , and it was observed that this separation line moved rearward as  $R_L$  increased. It was also observed that

the reattachment line originated near the tail of the body at a lower  $R_L$ . This reattachment line moved forward as  $R_L$  increased. Thus, this separation bubble decreased in size as  $R_L$  increased.

Based on these flow visualization observations and the drag coefficient results, the following deductions are made:

1. As  $R_L$  increased up to approximately  $7 \times 10^5$ , the laminar separation line moved very slowly rearward, with either no reattachment or reattachment close to the tail. The increasing length of the attached laminar boundary layer would decrease the skin-friction drag. This, combined with the reduction in wake size due to the rearward moving separation line, may have accounted for the gradual decrease in  $C_{D,\text{wet}}$  in this region.
2. For  $R_L > 7 \times 10^5$ , the reattachment line moved rapidly forward from the tail as the separation line moved slowly rearward. The values of  $C_{D,\text{wet}}$  subsequently decreased significantly as  $R_L$  increased through this region. This drastic decrease may have been attributable to the decreasing size of the separation bubble or the decreasing size of the wake or both.

The development and progression of the laminar separation bubble in this study was consistent with separation bubbles on airfoils as noted in reference 29. In reference 29, Roberts lists four possible flow regimes for airfoils with separation bubbles. These are

1. complete laminar separation at low values of  $R_L$
2. long bubble region as  $R_L$  increases
3. short bubble region as  $R_L$  increases further
4. transition prior to separation as  $R_L$  increases further

As noted, the first three regimes were present during this study.

References 29 and 30 point out that the velocity and pressure distributions on a body are increasingly affected as the bubble size increases. In addition, reference 31 points out that the turbulent boundary layer behind a separation bubble is thicker than the turbulent boundary layer for the case where there is smooth, attached flow without a bubble. This was also pointed out by Holmes (private communication from B. J. Holmes, NASA Langley Research Center, Hampton, Virginia). These factors help to substantiate the deduction above which relates the drastic decrease in  $C_{D,\text{wet}}$  to decreasing bubble size.

## Comparison With Other Data

As mentioned previously, this shape was also tested at the United States Naval Academy (refs. 17 and 18). For the present study, the desire was to test the model in the 13-in. MSBS up to  $M = 0.5$  to overlap the lower Reynolds number data from the Naval Academy. However, static aerodynamic stability problems exhibited by the model would not allow testing above  $M = 0.2$ . As a result, only one data point from this study overlaps the data from reference 18. However, the data may be compared by looking at the relative drag coefficient levels shown in figure 20. The tabular data from reference 18 are used for this comparison. Note the large discrepancy in  $C_{D,\text{wet}}$  at  $R_L = 1 \times 10^6$ . This discrepancy may be attributed to the fact that the data in reference 18 were not corrected for cavity pressure. In reference 18, Hoyt states that the corrections were not performed; however, he gives the necessary information and pressure measurements to correct the data for cavity pressure. Hoyt suggests using the following equation:

$$D_c = D_m - p_{cv} A_{tp}$$

where  $D_m$  and  $D_c$  are the measured and corrected drag forces and  $A_{tp}$  is the area inside the tail piece, which was 45 in<sup>2</sup>. The data from reference 18 were corrected with the above equation and the results are shown in figure 21. The corrected data are in good agreement with the results from the present study. The difference that still exists at  $R_L = 1 \times 10^6$  may be due to one or more of the following:

1. The sting at the rear of the model used at the Naval Academy may have acted as an extension of the body. This would have resulted in a higher fineness ratio which would have reduced the overall drag coefficient.
2. The sting divided and altered the wake region at the tail of the model, possibly reducing the overall drag.
3. The rear portion of the model used at the Naval Academy was slightly modified to accommodate the sting. This model did not have the slight flair at the tail, as was the case for the 13-in. MSBS model (see fig. 9). This slight modification may have altered the wake pattern.

Drag coefficient data on this laminar-flow body are also presented in reference 17. However, these drag coefficients do not agree with those in reference 18. The differences are not presently understood.

## Comparison of Free and Fixed Transition

Several runs with fixed transition were performed in an effort to assess the effect of fixing transition on the laminar separation bubble (ref. 32). Transition was fixed at two different locations with different grit sizes. Three-dimensional abrasive grain transition grit was used, with transition fixed at  $x/L = 0.17$  and  $0.50$ . The sizes of grit used were no. 100, no. 80, no. 60, and no. 40, which correspond to nominal grit diameters of  $0.006$ ,  $0.008$ ,  $0.012$ , and  $0.020$  in., respectively. Reference 33 was used to properly size the grit. Based on this technique, no. 60 and no. 80 grits were chosen for the  $x/L = 0.17$  station and no. 40 and no. 80 grits were chosen for the  $x/L = 0.50$  station. In addition, no. 40 and no. 100 grits were used at  $x/L = 0.17$  for comparison.

Figure 22 shows drag characteristics for the body with free and fixed transition. The fixed-transition data are for the no. 60 grit at  $x/L = 0.17$ . At the lowest Reynolds number, the boundary layer was thick, and the grit had no effect. However, as  $R_L$  increases to  $5 \times 10^5$ ,  $C_{D,\text{wet}}$  decreases drastically. This was a transitional region where the boundary layer was not yet fully turbulent beyond the grit. However, there was enough energy imparted from the grit to keep the boundary layer attached beyond the laminar separation line. Rearward movement of the separation line resulted in a lower  $C_{D,\text{wet}}$ . For  $R_L > 1 \times 10^5$ , the boundary layer was fully turbulent beyond the grit and the turbulent separation point moved much more slowly rearward with increasing  $R_L$ . This resulted in a much slower decrease in  $C_{D,\text{wet}}$  with increasing  $R_L$ . Figure 23 shows liquid crystal flow visualization results for this fixed transition case. Note the turbulent separation stations. The location was farther back on the model for the higher Reynolds number. As a comparison, the laminar separation station from figure 19 was at  $x/L = 0.63$ .

Figure 24 shows drag characteristics for fixed transition at  $x/L = 0.17$  for all four grit sizes. As the grit size decreases (grit number increases), the significant reduction in  $C_{D,\text{wet}}$  occurs at successively higher values of  $R_L$  because the smaller grit was less effective in fully tripping the thicker boundary layer at the lower Reynolds numbers. As  $R_L$  increased, the boundary layer thinned and the smaller grit effectively tripped the boundary layer to turbulent flow.

Figure 25 shows drag characteristics for free transition and for transition fixed at  $x/L = 0.50$  with two grit sizes. Transition was fixed at this location in order to retain laminar flow over a large portion of the body while laminar separation was avoided by making the boundary layer turbulent just ahead of

the separation bubble. It was also envisioned that tripping the boundary layer in this region would allow the turbulent boundary layer to remain attached farther on the body, thus resulting in a lower  $C_{D,\text{wet}}$ . The data in figure 25 show the same trends as those shown in figure 24. The smaller grit (no. 80) did not trip the boundary layer to fully turbulent flow until  $R_L = 1 \times 10^6$ . The larger grit (no. 40) appears to have effectively tripped the boundary layer through the entire Reynolds number range. In fact, at  $R_L > 8 \times 10^5$  the boundary layer had thinned to the point where the no. 40 grit was too large. This resulted in grit drag for Reynolds numbers greater than  $8 \times 10^5$ , with  $C_{D,\text{wet}}$  being larger for no. 40 grit than for no. 80 grit.

## Comparison With and Without Fins

A set of fins were installed in the tail of the model (see fig. 26) to assess their effectiveness in overcoming the static aerodynamic instabilities exhibited by the model at the higher Mach numbers. The fins did allow testing at higher speeds (up to  $M = 0.3$ ); thus, it was verified that the instabilities were aerodynamic. The increase in drag coefficient for the model with fins compared with that for the model without fins is shown in figure 27. The change in  $C_{D,\text{wet}}$  is relatively constant except at the higher Reynolds numbers, where the increase is greater.

Figure 28 shows drag characteristics for free and fixed transition for the finned model. Transition was fixed at  $x/L = 0.50$  with no. 80 grit. A comparison of these data with fixed-transition data (same grit size) from figure 25 shows large differences at the higher Reynolds numbers. These differences may have been due to an altered flow pattern for the finned model as a result of the interaction of the fins with the thick turbulent boundary layer at the model tail.

## Comparison of Experimental and Computational Results

### SANDRAG Code

A comparison of the drag coefficient results from SANDRAG with the free-transition data generally indicates a large discrepancy between theory and experiment. (See fig. 29.) Further insight into the computational results is given in figure 30, which shows a breakdown of the various drag coefficient components and their contributions to the overall drag coefficient. For a given shape, SANDRAG breaks down the overall drag into four components: skin-friction drag, base pressure drag, pressure drag, and separation drag. The base pressure drag is simply the computed base pressure coefficient multiplied by the ratio

of the base area to the reference area. The pressure drag is the drag based on the pressure distribution around the portion of the body that has unseparated flow. Note that there is not a separation drag component for the laminar-flow body in figure 30. At the lower Reynolds numbers ( $R_L < 7 \times 10^5$ ), part of the discrepancy in figure 29 may be attributable to the lack of separation drag in the computation. This is the drag based on the pressure in the separated flow region. Recall from previous discussions that the boundary layer may have separated completely in this Reynolds number range. Also note that the experimental and computational results approach each other as  $R_L$  increases, as shown in figure 29. This may be attributable to the decreasing bubble size with increasing  $R_L$ . From previous discussions, it appeared that  $C_{D,\text{wet}}$  decreased as the bubble size decreased because of a decreasing separation drag component.

The code did predict a separation bubble on the body in the turbulent-boundary-layer region following transition. However, it did not calculate a pressure drag contribution from this bubble. (Separation drag is only calculated when the flow does not reattach.) It appeared from the flow visualizations that the separation point was in the laminar region, in which case transition actually occurs on the bubble (ref. 30). Boundary-layer transition on the bubble would result in a thicker boundary layer in the turbulent region when compared with transition occurring prior to the bubble. This thicker boundary layer would result in a larger momentum deficit at the model tail and, consequently, a higher drag coefficient.

The code also predicted that the bubble would decrease in size as  $R_L$  increased. This trend was also observed with the oil flow visualization. Figure 31 shows the predictions of turbulent separation and reattachment points for this bubble. Note the differences between the locations of the experimental and computational bubbles by comparing the oil flow results from figure 18 with the computational results in figure 31. At  $R_L = 1.2 \times 10^6$ , the oil flow separation line was at  $x/L = 0.67$  and the reattachment line was at  $x/L = 0.73$ . The computational separation point was  $x/L = 0.835$  and the reattachment point was  $x/L = 0.878$ .

### Nakayama and Patel Code

As noted previously, this code calculates the skin-friction portion of the drag. It does not account for pressure drag, such as separation and base drag. Because of this, the predicted  $C_{D,\text{wet}}$  values are low, as shown in figure 32. These predicted  $C_{D,\text{wet}}$  values

are very close to the skin-friction drag coefficients from SANDRAG shown in figure 30.

For this study, two different empirical correlations incorporated in the code were used to predict transition locations. One correlation is from Granville (ref. 34) and the other is from van Driest and Blumer (ref. 35). With Granville's criterion, this code predicted laminar separation prior to transition, with a laminar separation location of  $x/L = 0.67$  predicted for the entire Reynolds number range. The code assumes immediate reattachment of the turbulent boundary layer. With van Driest and Blumer's criterion, the code predicted transition at  $x/L = 0.66$  for the entire Reynolds number range. The code did not predict separation with this criterion. As shown in figure 32, both criteria give essentially the same drag coefficient results.

A comparison is also made with some of the fixed-transition data by incorporating the experimental transition location into the code. This comparison is shown in figure 33, where the data are from figure 25 (no. 40 grit at  $x/L = 0.50$ ) and the computational results are based on a transition location of  $x/L = 0.50$ . The predicted  $C_{D,\text{wet}}$  values are close to the experimental data. The differences are greater at the higher Reynolds numbers because of increasing grit drag for the experimental data. The computational results are fairly accurate in this case even though the code calculates skin-friction drag only. If the flow was fully attached and if the base drag contribution was small, then skin-friction drag would dominate and a good correlation between theory and experiment would be expected. However, the flow is not fully attached in this case, as is shown in figure 34, which is a liquid crystal flow visualization photograph showing turbulent separation at  $x/L = 0.80$ . One possible scenario is that the drag for this fixed-transition case is so dominated by skin-friction drag that the base and separation drag components are very small in comparison.

### Conclusions

The primary objective of this research was met by substantiating the drag-force measuring capabilities of the 13-in. Magnetic Suspension and Balance System. The drag-force calibrations were very repeatable, with no significant hysteresis. The root mean square (rms) of the errors for the initial calibration was small at 0.11 percent of the full-scale calibration load. Wind-on drag-force measurements showed excellent repeatability, with the rms of the differences between two sets of data at only 0.58 percent of the full-scale calibration load.

The free-transition values of drag coefficient  $C_{D,\text{wet}}$  for the laminar-flow body generally decreased

with increasing Reynolds number  $R_L$ . The drastic drop in  $C_{D,\text{wet}}$  at the higher  $R_L$  values appears to have been directly related to the decreasing size of the laminar separation bubble through this Reynolds number region. Comparisons of these data with data on general streamlined bodies showed similar trends. Comparisons with other data (corrected for cavity pressure) for the same shape showed a consistent level and trend with Reynolds number.

Tests with transition fixed generally showed a reduction in drag coefficient because of elimination of the laminar separation bubble. Fixing transition at the 50-percent model length station with no. 80 grit gave the lowest  $C_{D,\text{wet}}$  value for these investigations. A further reduction in  $C_{D,\text{wet}}$  may be obtained by fixing transition just ahead of the laminar separation line. This lower drag coefficient would result from a longer run of laminar flow on the body prior to transition.

The model exhibited aerodynamic instabilities that did not allow testing above a Mach number of 0.2. A set of fins installed in the model tail allowed

testing up to a Mach number of 0.3; thus, it was verified that the instabilities were aerodynamic. As expected, the drag coefficients with fins were higher.

Surface flow visualization through the use of both liquid crystals and pigmented oil flow verified the existence and location of the laminar separation bubble. The oil flow was especially useful in highlighting the separation and reattachment lines.

Comparisons with two simple computational drag prediction schemes were generally poor. These codes were developed to predict drag for simple axisymmetric shapes; they were not designed to accurately predict drag for complicated axisymmetric shapes with separated flow, such as the one used in this study. Proper modeling of the laminar separation bubble and the transition location on this bubble are essential to achieve accurate drag prediction in this case.

NASA Langley Research Center  
Hampton, VA 23665-5225  
February 23, 1989

## Appendix

### Data Reduction and Corrections

#### Drag-Force Equation

When a soft iron core is used, a drag-force calibration curve fit from the 13-in. MSBS takes the following form:

$$D = AI^2 + BI + C \quad (\text{A1})$$

The coefficients  $A$ ,  $B$ , and  $C$  change for different models or cores and/or different locations of the model or core in the electromagnetic fields.

During a typical drag-force calibration for this study, the first data point was taken with a 5-gf weight attached to the calibration line. To get the drag electromagnet current value for a zero axial load, equation (A1) was solved with the quadratic formula. This formula is defined as

$$I = \frac{-B \pm \sqrt{B^2 - 4AC}}{2A} \quad (\text{A2})$$

The positive root  $I_0$  is the drag electromagnet current value for a zero axial load.

When the wind-on drag currents are converted to equivalent forces, a delta current is initially obtained for each data point from

$$\Delta I = I_{\text{wo}} - I_{\text{woff},0} \quad (\text{A3})$$

The corrected current for each data point is then defined as

$$I_c = I_0 + \Delta I \quad (\text{A4})$$

The drag force was computed with  $I_c$  used in equation (A1). This corrected current was used to compensate for possible wind-off current zero shifts.

#### Buoyancy Corrections

Three-dimensional buoyancy corrections were applied to the drag-force data with the following equation from reference 36:

$$\Delta D_B = -\frac{\pi}{4} \lambda t^3 \frac{dp}{dl} \quad (\text{A5})$$

The  $\lambda$  term for a body of revolution is defined as

$$\lambda = 4 \int \frac{v}{V} \frac{[z(s)]^2}{t^3} ds \quad (\text{A6})$$

This constant term was calculated from the potential solution results from the computer code SANDRAG. The value of  $\lambda$  for the laminar-flow body was 2.6994. For the  $\frac{dp}{dl}$  term, tunnel-empty pressure measurements were taken along the centerline of one of the vertical test section walls. This pressure gradient varied with tunnel speed; therefore, a curve fit of  $\frac{dp}{dl}$  as a function of  $M$  was used when these corrections were applied to the data.

#### Blockage Corrections

Both solid and wake blockage corrections (ref. 37) were applied to the results of this study. The blockage factor is defined as

$$\epsilon_b = \epsilon_{s'} + \epsilon_w \quad (\text{A7})$$

The solid blockage term  $\epsilon_{s'}$  for three-dimensional models in rectangular test sections is defined as

$$\epsilon_{s'} = \tau \left( \frac{A_m}{bh} \right)^{3/2} \frac{1}{\beta^3} \lambda \quad (\text{A8})$$

The  $\tau$  term is defined as

$$\tau = \frac{1}{2\pi^{3/2}} \sum_{m=-\infty}^{\infty} \sum_{n=-\infty}^{\infty} \left( \frac{bh}{m^2 b^2 + n^2 h^2} \right)^{3/2} \quad (\text{A9})$$

except for  $(m, n) = (0, 0)$ . This equation gives a value of  $\tau$  for a rectangular test section of width  $b$  and height  $h$ . For this investigation, the test section shape was a modified octagon which can be considered a rectangle with fillets. In reference 38, Batchelor showed that the value of  $\tau$  for a 7- by 9-ft rectangular test section with fillets (similar to the shape used with this investigation) is very close to the value of  $\tau$  for the basic rectangle. Therefore, for this study the value of  $\tau$  was assumed to be the value of the basic rectangle. The basic rectangle is 12.56 by 10.69 in. and  $\tau$  is 0.818.

The wake blockage term  $\epsilon_w$  for three-dimensional models in rectangular test sections is defined as

$$\epsilon_w = \frac{1}{4} \frac{S}{bh} \left( \frac{1 + 0.4M^2}{\beta^2} \right) C_{D,0} \quad (\text{A10})$$

For this study, equations (A8) and (A10) were used with  $bh$  replaced by the cross-sectional area of the test section. This modification is suggested in reference 37 as an approximation for octagonal test sections.

## References

1. Tuttle, Marie H.; and Gloss, Blair B.: *Support Interference of Wind Tunnel Models—A Selective Annotated Bibliography*. NASA TM-81909, 1981. (Corrected 1988.)
2. Tuttle, Marie H.; and Lawing, Pierce L.: *Support Interference of Wind Tunnel Models—A Selective Annotated Bibliography*. Supplement to NASA TM-81909, 1984. (Corrected 1988.)
3. Lawing, Pierce L.; Dress, David A.; and Kilgore, Robert A.: *Potential Benefits of Magnetic Suspension and Balance Systems*. NASA TM-89079, 1987.
4. Basmajian, V. V.; Copeland, A. B.; and Stephens, T.: *Studies Related to the Design of a Magnetic Suspension and Balance System*. NASA CR-66233, 1966.
5. Boyden, Richmond P.; Britcher, Colin P.; and Tcheng, Ping: Status of Wind Tunnel Magnetic Suspension Research. SAE Tech. Paper Ser. 851898, Oct. 1985.
6. Tournier, M.; and Laurenceau, P.: Suspension Magnétique d'une Maquette en Soufflerie. *Recherche Aeronaut.*, no. 59, July–Aug. 1957, pp. 21–26.
7. Tuttle, Marie H.; Kilgore, Robert A.; and Boyden, Richmond P.: *Magnetic Suspension and Balance Systems—A Selected, Annotated Bibliography*. NASA TM-84661, 1983. (Supersedes NASA TM-80225.)
8. Britcher, C.; Goodyer, M. J.; Scurlock, R. G.; and Wu, Y. Y.: A Flying Superconducting Magnet and Cryostat for Magnetic Suspension of Wind-Tunnel Models. *Cryogenics*, vol. 24, no. 4, Apr. 1984, pp. 185–189.
9. Bloom, H. L.; et al.: *Design Concepts and Cost Studies for Magnetic Suspension and Balance Systems*. NASA CR-165917, 1982.
10. Boom, R. W.; Eyssa, Y. M.; McIntosh, G. E.; and Abdelsalam, M. K.: *Magnetic Suspension and Balance System Study*. NASA CR-3802, 1984.
11. Boom, R. W.; Eyssa, Y. M.; McIntosh, G. E.; and Abdelsalam, M. K.: *Magnetic Suspension and Balance System Advanced Study*. NASA CR-3937, 1985.
12. Matthews, R. K.; Brown, M. D.; and Langford, J. M.: *Description and Initial Operation of the AEDC Magnetic Model Suspension Facility: Hypersonic Wind Tunnel (E)*. AEDC-TR-70-80, U.S. Air Force, May 1970. (Available from DTIC as AD 869 634.)
13. Britcher, Colin P.: *User Guide for the Digital Control System of the NASA/Langley Research Center's 13-Inch Magnetic Suspension and Balance System*. NASA CR-178210, 1987.
14. Tcheng, Ping; and Schott, Timothy D.: A Five Component Electro-Optical Positioning System. *ICIASF '87 Record—International Congress on Instrumentation in Aerospace Simulation Facilities*, 87CH2449-7, Inst. of Electrical and Electronics Engineers, Inc., 1987, pp. 322–333.
15. Johnson, William G., Jr.; and Dress, David A.: *The 13-Inch Magnetic Suspension and Balance System Wind Tunnel*. NASA TM-4090, 1989.
16. Parsons, Jerome S.; Goodson, Raymond E.; and Goldschmied, Fabio R.: Shaping of Axisymmetric Bodies for Minimum Drag in Incompressible Flow. *J. Hydronaut.*, vol. 8, no. 3, July 1974, pp. 100–107.
17. Hansen, R. J.; and Hoyt, J. G.: Laminar-to-Turbulent Transition on a Body of Revolution With an Extended Favorable Pressure Gradient Forebody. *J. Fluids Eng.*, vol. 106, no. 2, June 1984, pp. 202–210.
18. Hoyt, John G., III: *Preliminary Resistance Test of Laminar Flow Submersible*. USNAHL Lab. Note HL-88-6, U.S. Naval Academy, Dec. 1988.
19. Dodbele, S. S.; van Dam, C. P.; Vijgen, P. M. H. W.; and Holmes, B. J.: Shaping of Airplane Fuselages for Minimum Drag. AIAA-86-0316, Jan. 1986.
20. Dodbele, S. S.; van Dam, C. P.; and Vijgen, P. M. H. W.: *Design of Fuselage Shapes for Natural Laminar Flow*. NASA CR-3970, 1986.
21. Holmes, Bruce J.; Gall, Peter D.; Croom, Cynthia C.; Manuel, Gregory S.; and Kelliher, Warren C.: *A New Method for Laminar Boundary Layer Transition Visualization in Flight—Color Changes in Liquid Crystal Coatings*. NASA TM-87666, 1986.
22. Gall, P. D.; and Holmes, B. J.: Liquid Crystals for High-Altitude In-Flight Boundary Layer Flow Visualization. AIAA-86-2592, Sept.–Oct. 1986.
23. Holmes, Bruce J.; and Obara, Clifford J.: Advances in Flow Visualization Using Liquid-Crystal Coatings. SAE Tech. Paper Ser. 871017, Apr. 1987.
24. Wolfe, Walter P.; and Oberkampf, William L.: Drag Prediction for Projectiles and Finned Bodies in Incompressible Flow. AIAA-85-0104, Jan. 1985.
25. Wolfe, Walter P.; and Oberkampf, William L.: *SANDRAG—A Computer Code for Predicting Drag of Bodies of Revolution at Zero Angle of Attack in Incompressible Flow*. SAND85-0515 (Contract DE-AC04-76DP00789), Sandia National Lab., Apr. 1985.
26. Nakayama, A.; and Patel, V. C.: Calculation of the Viscous Resistance of Bodies of Revolution. *J. Hydronaut.*, vol. 8, no. 4, Oct. 1974, pp. 154–162.
27. Patel, V. C.: A Simple Integral Method for the Calculation of Thick Axisymmetric Turbulent Boundary Layers. *Aeronaut. Q.*, vol. 25, pt. 1, Feb. 1974, pp. 47–58.
28. Hoerner, Sighard F.: *Fluid-Dynamic Drag*. Hoerner Fluid Dynamics (Brick Town, New Jersey), c.1965.
29. Roberts, W. B.: Calculation of Laminar Separation Bubbles and Their Effect on Airfoil Performance. AIAA Paper 79-0285, Jan. 1979.
30. Horton, H. P.: *Laminar Separation Bubbles in Two and Three Dimensional Incompressible Flow*. Ph.D. Thesis, Queen Mary College, Univ. of London, 1968.
31. Weibust, E.; Bertelrud, A.; and Ridder, S. O.: Experimental and Theoretical Analysis of Laminar Separation Bubbles. AIAA-84-2201, Aug. 1984.
32. Mueller, Thomas J.; and Batill, Stephen M.: Experimental Studies of Separation on a Two-Dimensional Airfoil at Low Reynolds Numbers. *AIAA J.*, vol. 20, no. 4, Apr. 1982, pp. 457–463.
33. Braslow, Albert L.; and Knox, Eugene C.: *Simplified Method for Determination of Critical Height of Distributed Roughness Particles for Boundary-Layer Transition at Mach Numbers From 0 to 5*. NACA TN 4363, 1958.
34. Granville, Paul S.: *The Calculation of the Viscous Drag of Bodies of Revolution*. Rep. 849, David W. Taylor Model Basin, July 1953.

35. Van Driest, E. R.; and Blumer, C. B.: Boundary Layer Transition: Freestream Turbulence and Pressure Gradient Effects. *AIAA J.*, vol. 1, no. 6, June 1963, pp. 1303-1306.
36. Glauert, H.: *Wind-Tunnel Interference on Wings, Bodies and Airscrews*. R. & M. No. 1566, British Aeronautical Research Council, 1933.
37. Garner, H. C.; Rogers, E. W. E.; Acum, W. E. A.; and Maskell, E. C.: *Subsonic Wind Tunnel Wall Corrections*. AGARD-AG-109, Oct. 1966.
38. Batchelor, G. K.: *Interference on Wings, Bodies and Airscrews in a Closed Tunnel of Octagonal Section*. Rep. ACA-5, Australian Council for Aeronautics, Mar. 1944.

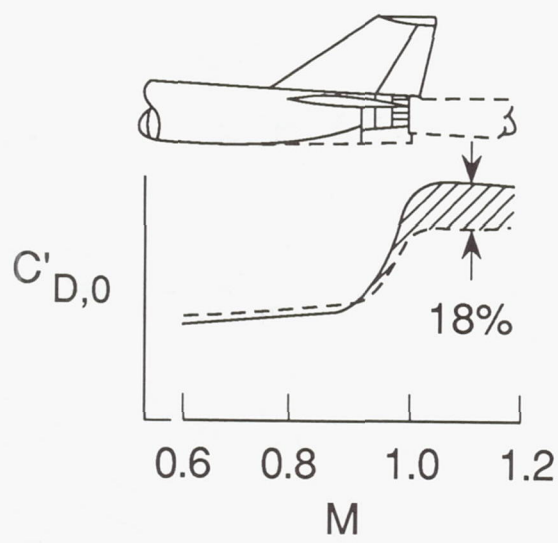
Table I. Model Coordinates for Laminar-Flow Body of Revolution

<i>x</i> , in.	<i>r</i> , in.	<i>x</i> , in.	<i>r</i> , in.
0.0000	0.0000	5.8000	1.3164
.0010	.0163	6.0000	1.3243
.0020	.0231	6.2000	1.3284
.0040	.0327	6.4000	1.3317
.0060	.0400	6.6000	1.3332
.0080	.0462	6.6660	1.3333
.0100	.0517	6.8000	1.3329
.0150	.0634	7.0000	1.3297
.0200	.0732	7.2000	1.3225
.0250	.0819	7.4000	1.3100
.0300	.0898	7.6000	1.2910
.0400	.1037	7.8000	1.2645
.0500	.1161	8.0000	1.2300
.0600	.1273	8.2000	1.1868
.0700	.1377	8.4000	1.1348
.0800	.1474	8.5000	1.1055
.0900	.1565	8.6000	1.0740
.1000	.1651	8.7000	1.0404
.2000	.2359	8.8000	1.0048
.3000	.2917	8.9000	.9673
.4000	.3399	9.0000	.9280
.5000	.3832	9.1000	.8872
.6000	.4232	9.2000	.8449
.7000	.4605	9.3000	.8015
.8000	.4958	9.4000	.7571
.9000	.5293	9.4500	.7346
1.0000	.5614	9.5000	.7120
1.2000	.6218	9.5500	.6894
1.4000	.6781	9.6000	.6667
1.6000	.7308	9.6500	.6440
1.8000	.7805	9.7000	.6215
2.0000	.8274	9.7500	.5994
2.2000	.8717	9.8000	.5778
2.4000	.9136	9.8500	.5569
2.6000	.9532	9.9000	.5368
2.8000	.9907	10.0000	.4994
3.0000	1.0259	10.1000	.4663
3.2000	1.0592	10.2000	.4378
3.4000	1.0904	10.3000	.4141
3.6000	1.1196	10.4000	.3953
3.8000	1.1468	10.5000	.3811
4.0000	1.1722	10.6000	.3713
4.2000	1.1956	10.7000	.3654
4.4000	1.2172	10.8000	.3629
4.6000	1.2369	11.0000	.3659
4.8000	1.2547	11.2000	.3752
5.0000	1.2707	11.4000	.3861
5.2000	1.2849	11.6000	.3947
5.4000	1.2972	11.8000	.3992
5.6000	1.3077	12.0000	.4000

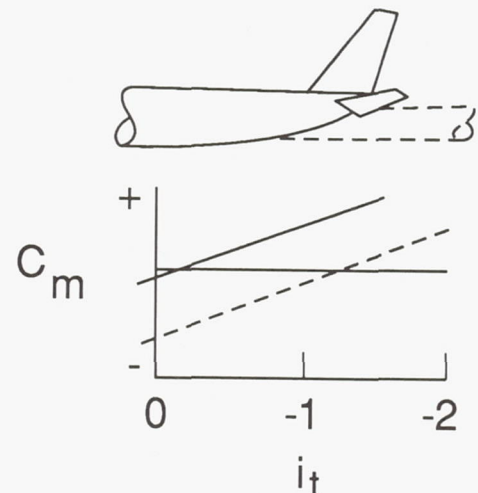
Table II. Drag Coefficients for Laminar-Flow Body of Revolution (Run 1)

$R_L$	$C_{D,\text{wet}}$	
	Uncorrected	Corrected
$3.645 \times 10^5$	$1.333 \times 10^{-2}$	$1.179 \times 10^{-2}$
4.376	1.351	1.201
5.047	1.297	1.155
5.608	1.259	1.121
6.894	1.181	1.050
7.290	1.152	1.023
7.972	1.094	.969
8.482	1.044	.922
8.964	.972	.854
9.406	.900	.786
10.071	.783	.675
10.775	.698	.594
11.159	.647	.546
11.538	.623	.523
12.199	.583	.485
12.575	.548	.451
12.979	.562	.465
13.405	.548	.451

- Afterbody drag



- Trim and tail loads



- Yaw damping

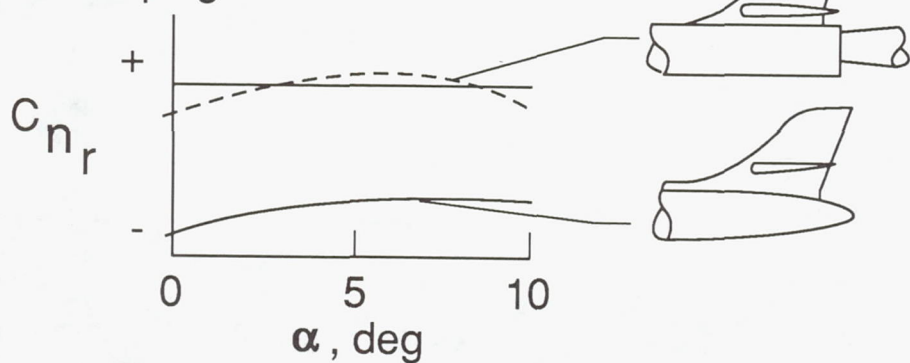
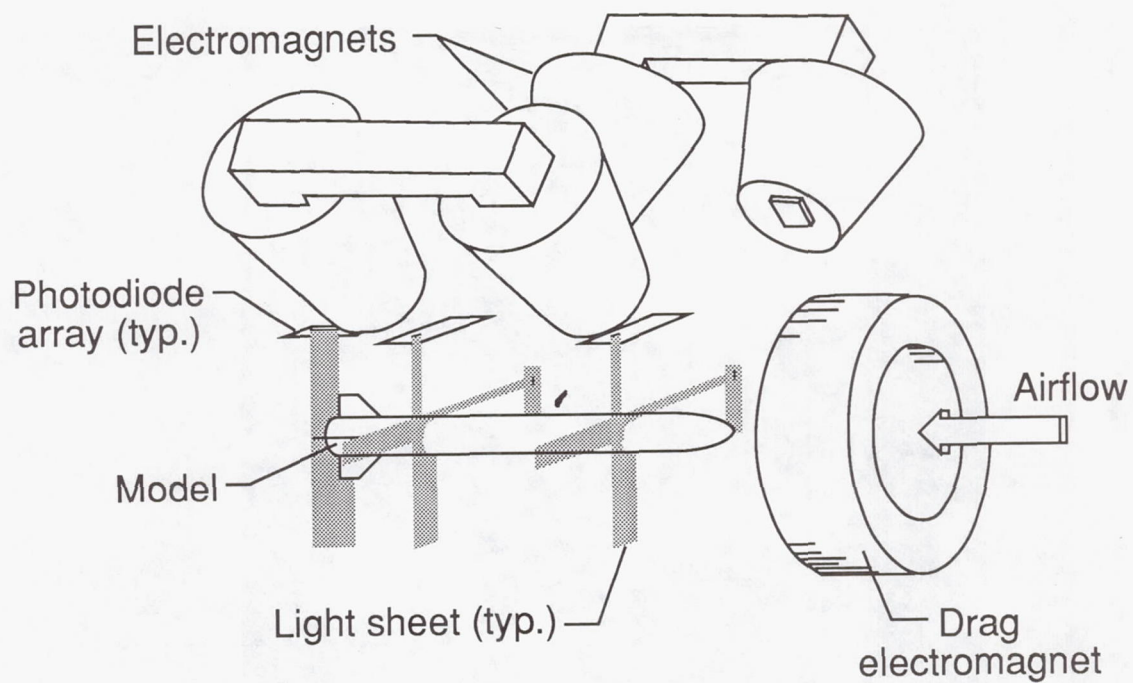
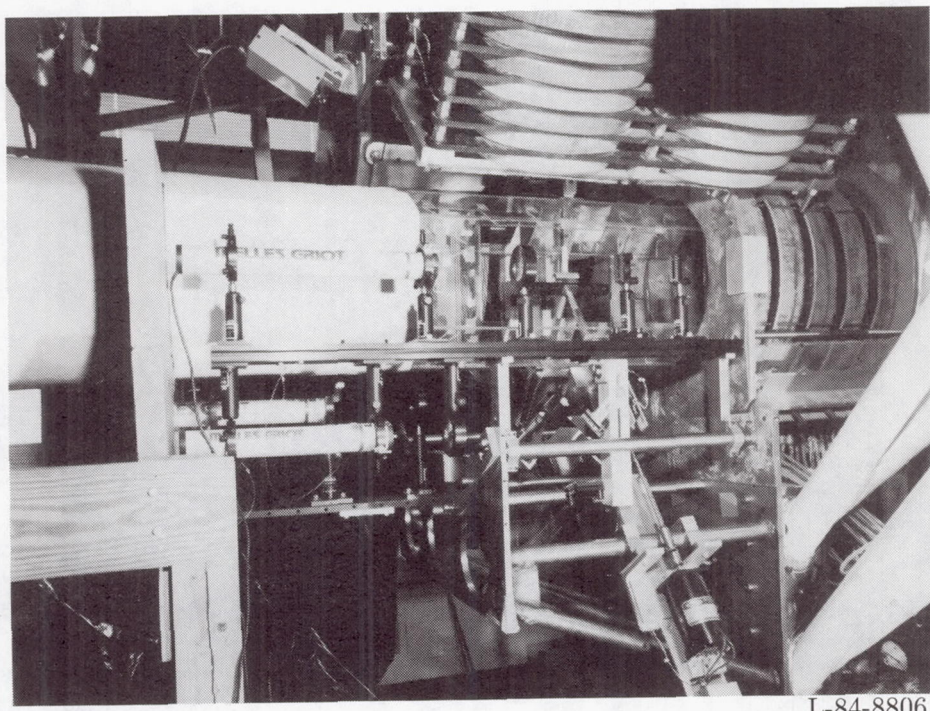


Figure 1. Examples of model support interference problems.

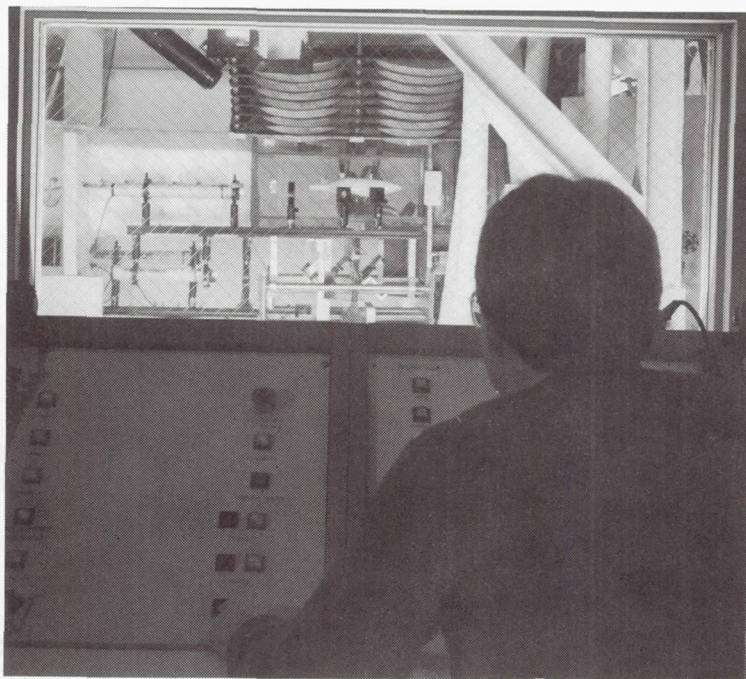


(a) Sketch.



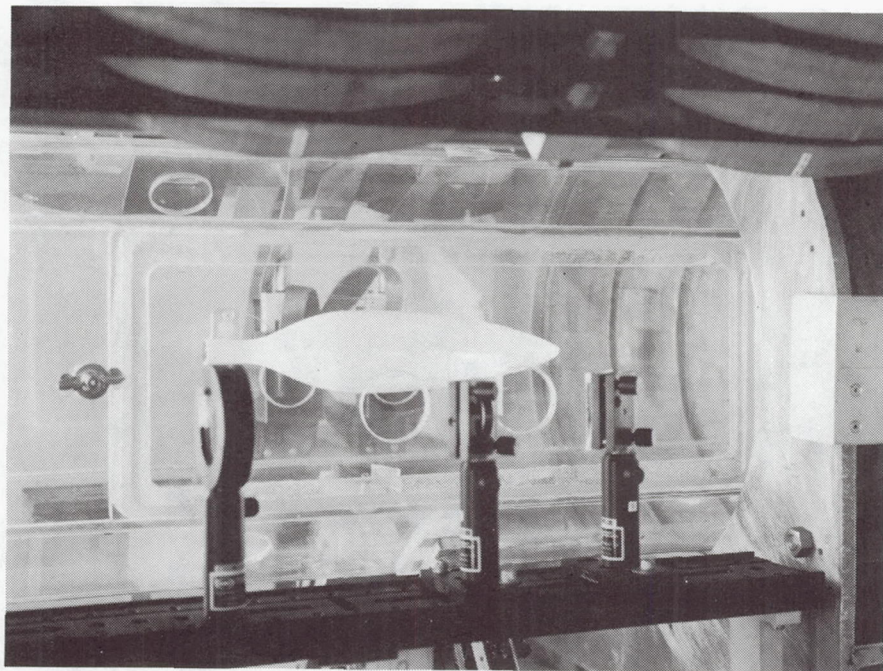
(b) Photograph.

Figure 2. Arrangement of 13-in. MSBS.



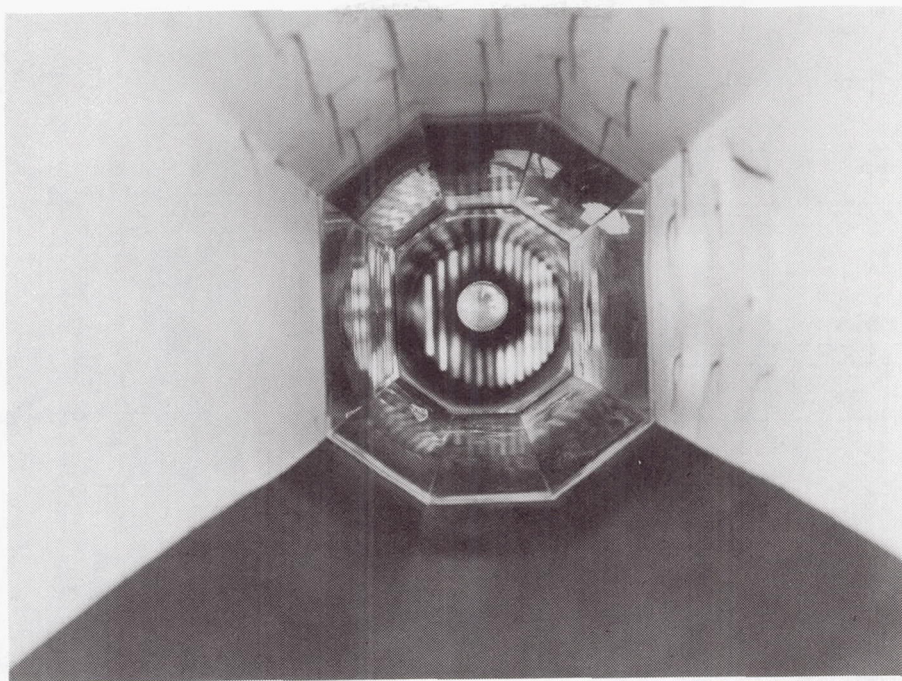
L-86-11,940

Figure 3. View from control room of 13-in. MSBS.



L-86-11,936

Figure 4. Laminar-flow body suspended in 13-in. MSBS.



L-86-11,941

Figure 5. View from contraction section of wind tunnel of laminar-flow body suspended in 13-in. MSBS.

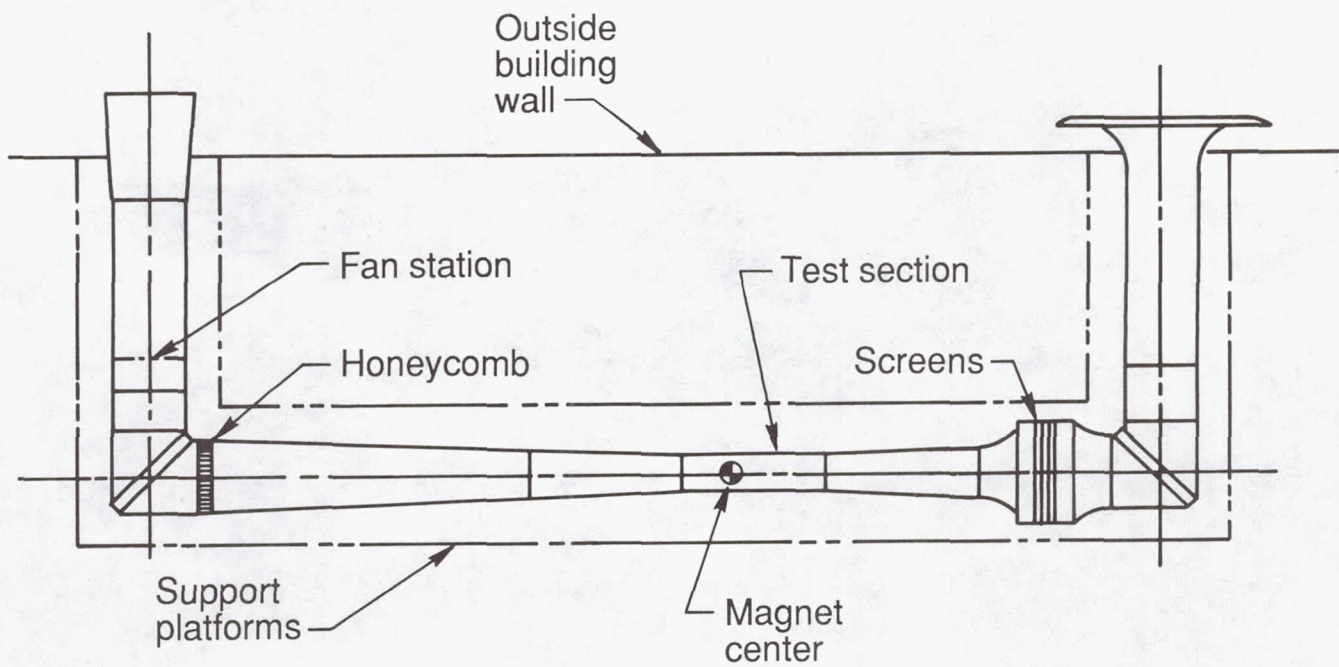


Figure 6. Layout of 13-in. MSBS wind tunnel.

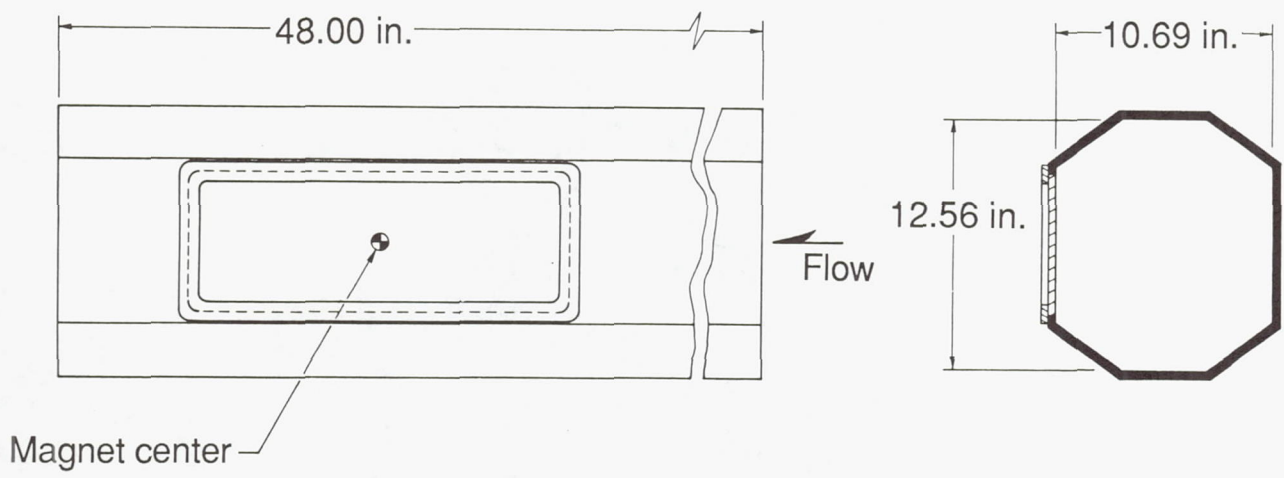
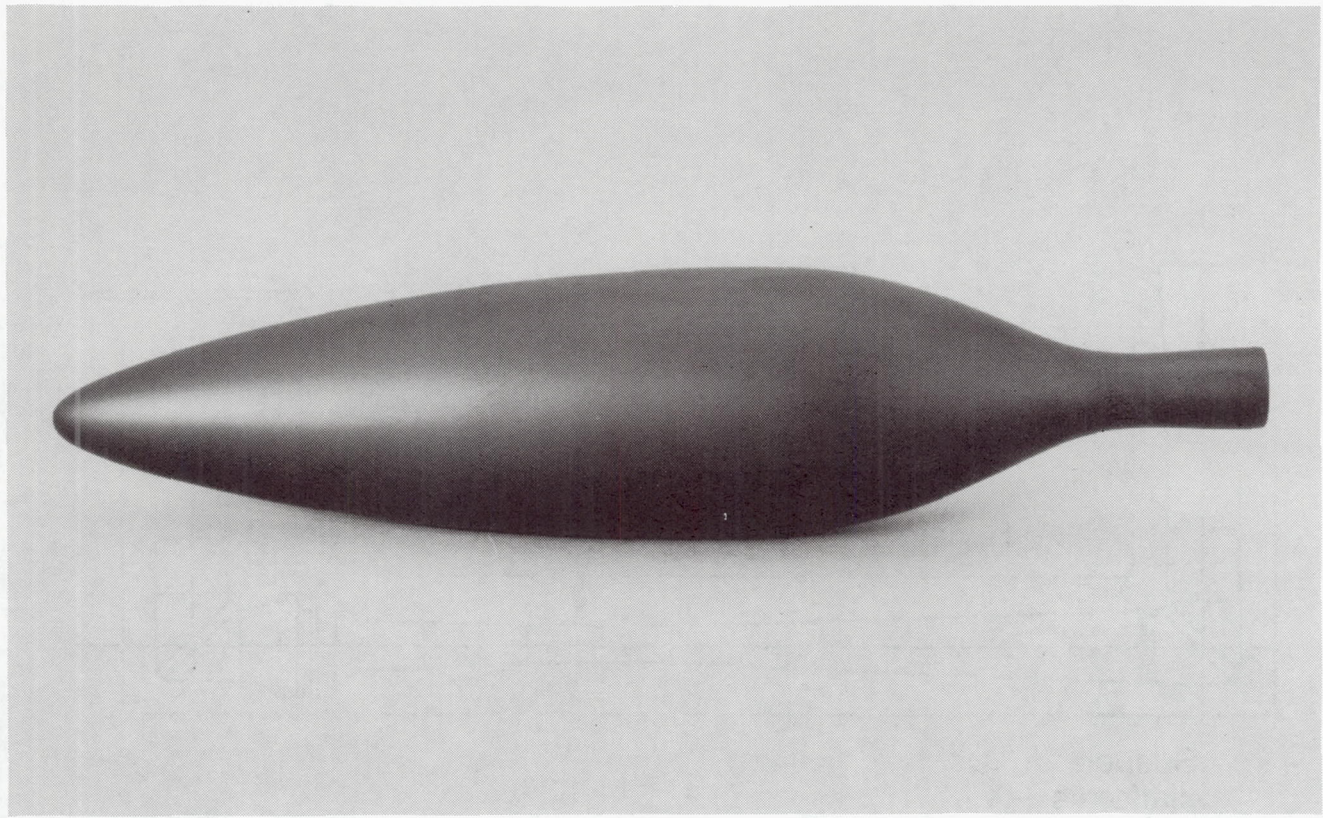


Figure 7. Test section of 13-in. MSBS wind tunnel.



L-87-11,132

Figure 8. Laminar-flow model used in 13-in. MSBS.

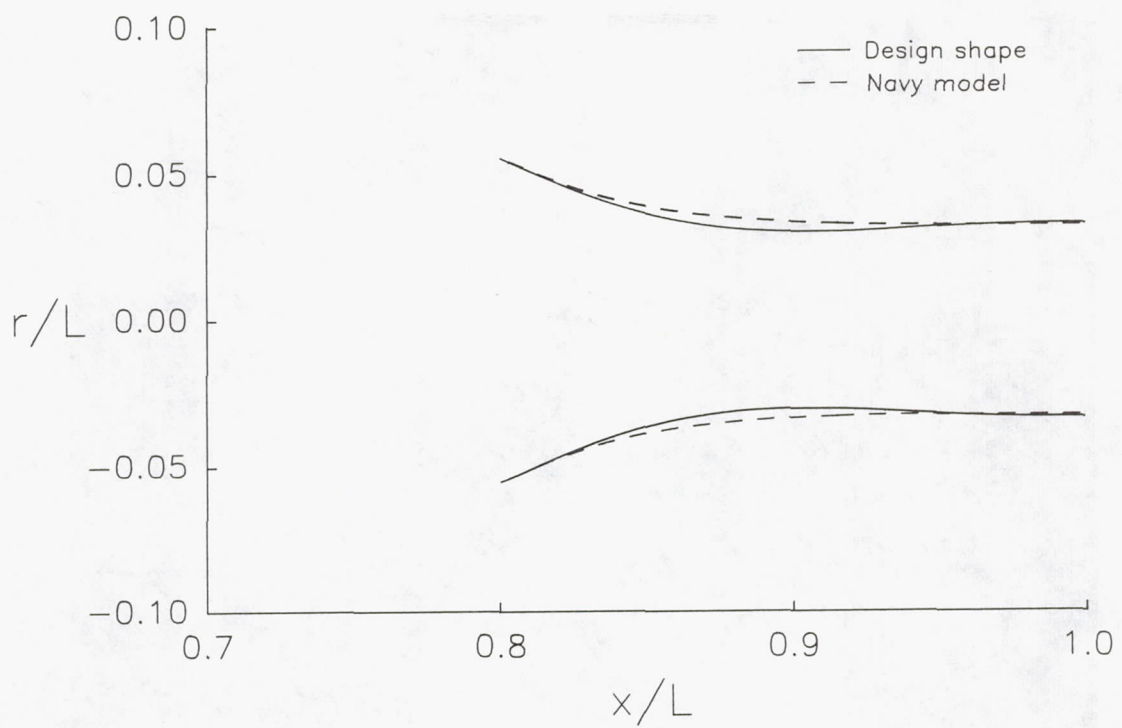


Figure 9. Tail modification of Navy model from design shape.

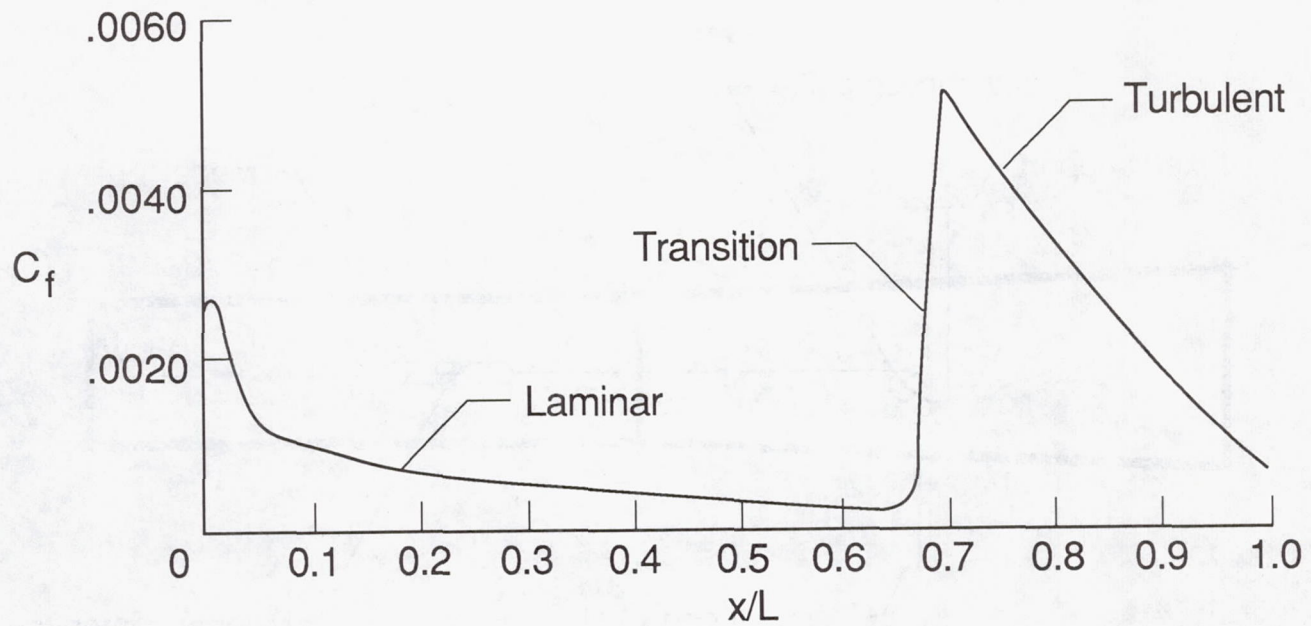
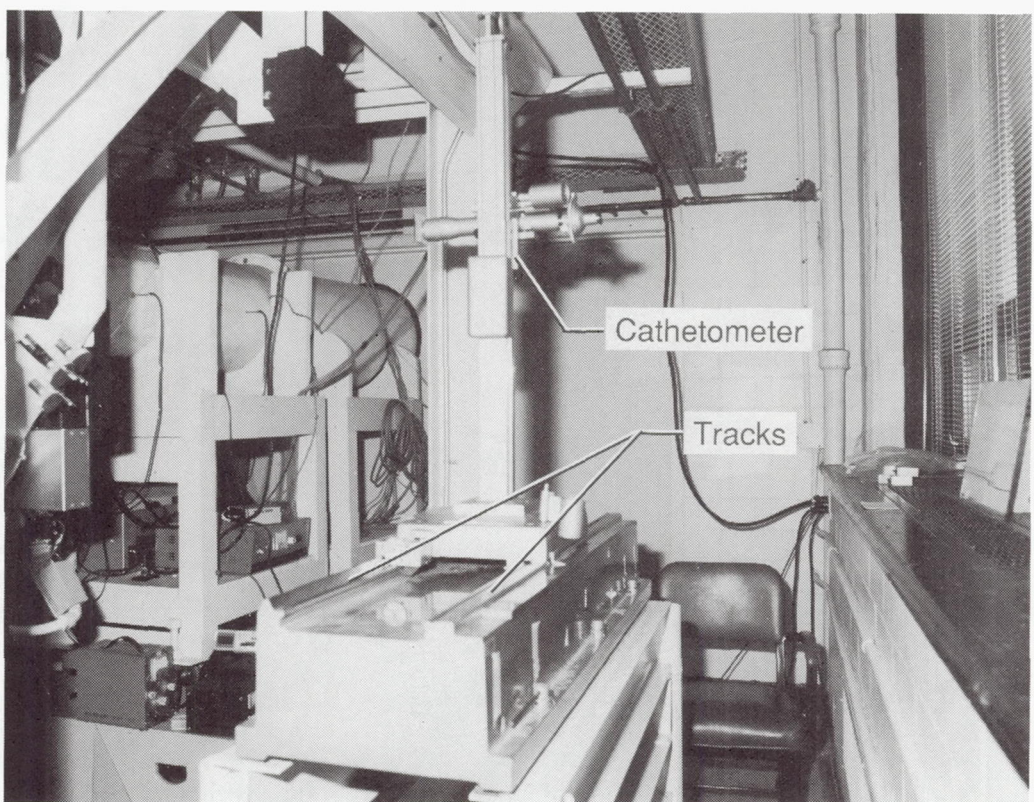


Figure 10. Skin-friction coefficient for typical natural laminar-flow airfoil. (From ref. 23.)



L-87-8070

Figure 11. Optical cathetometer on tracks.

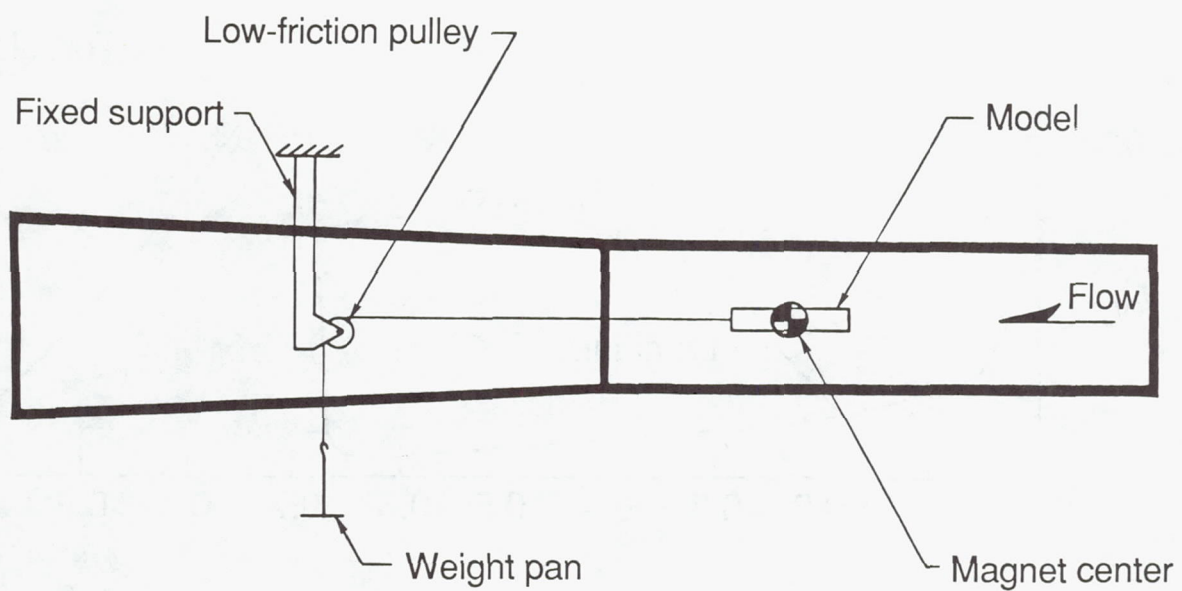
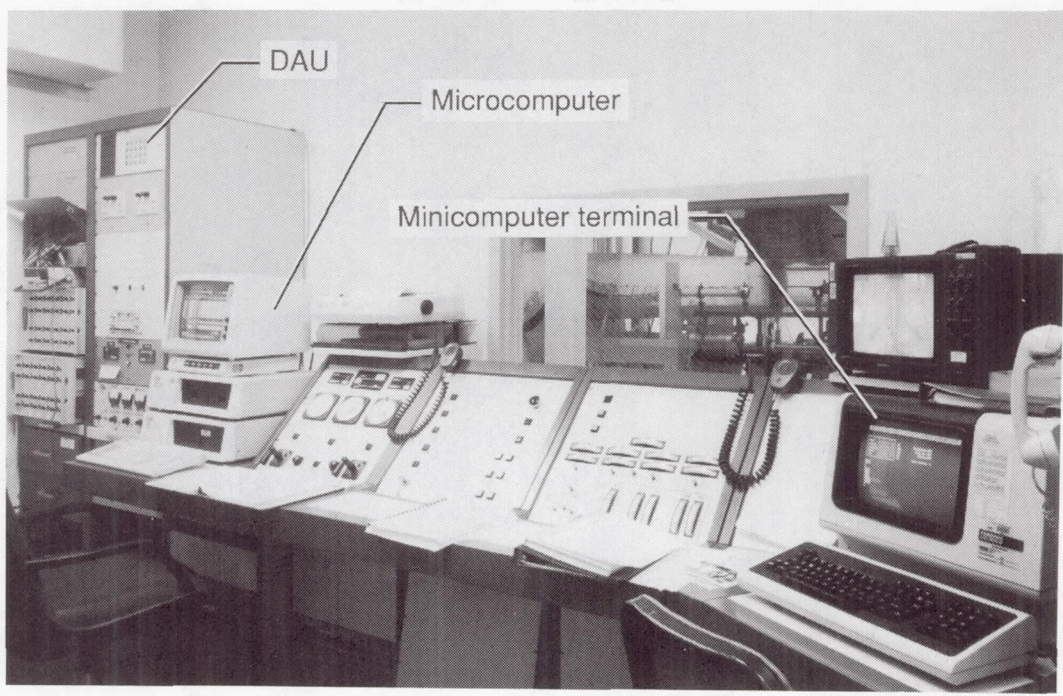


Figure 12. Drag calibration setup.



L-87-8941

Figure 13. Control room used for data acquisition.

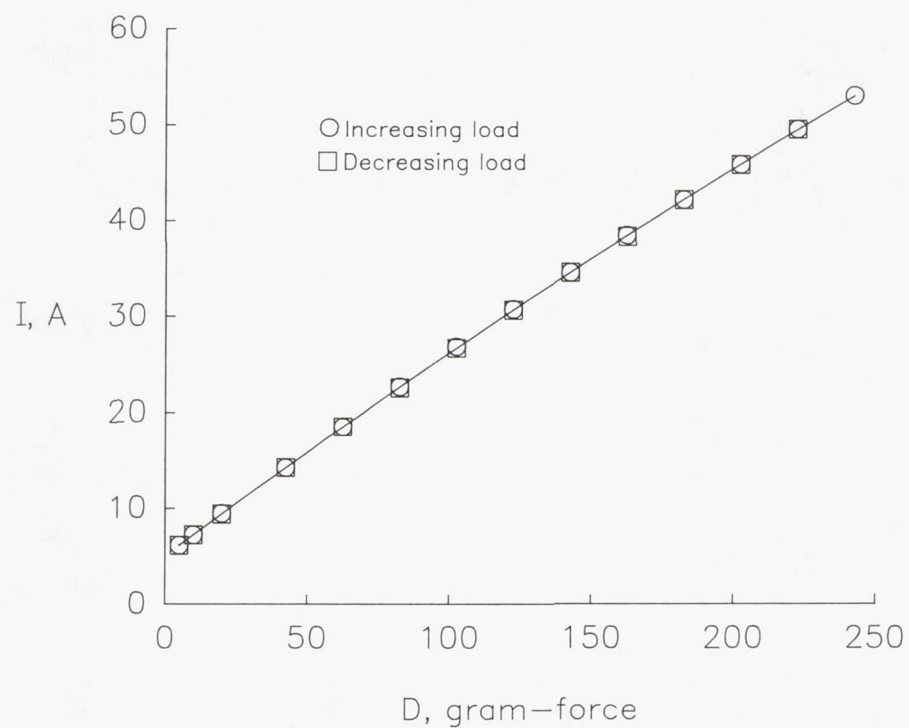


Figure 14. Drag-force calibration for laminar-flow body.

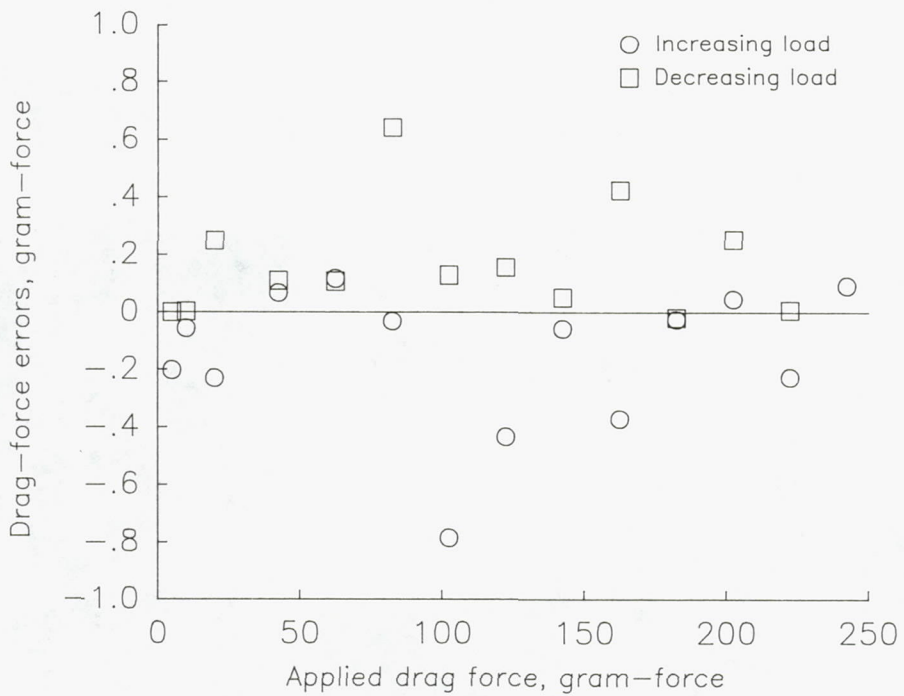


Figure 15. Drag-force errors from calibration of laminar-flow body.

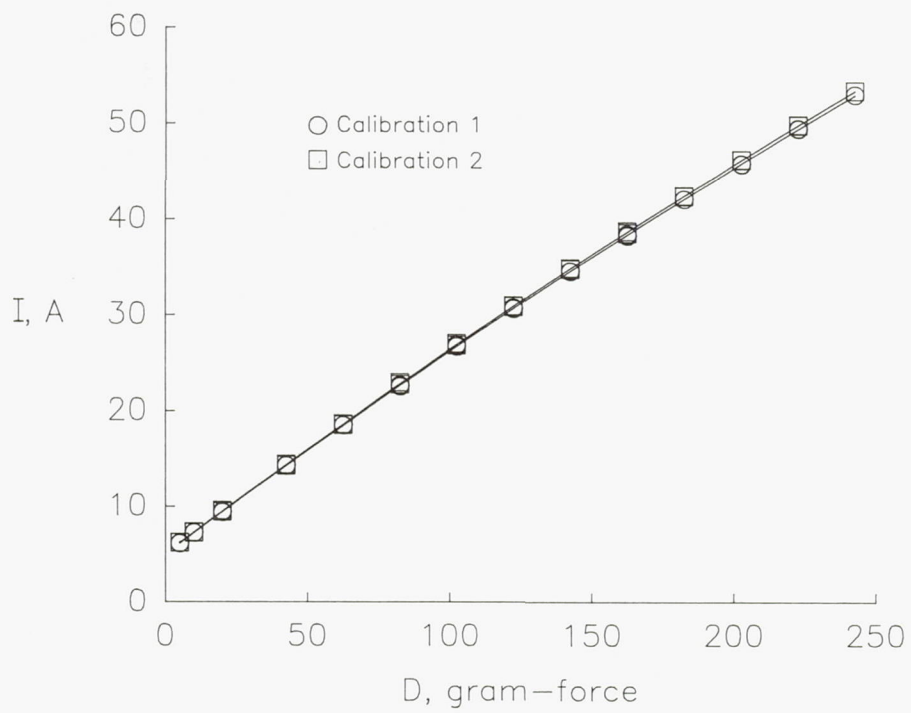


Figure 16. Repeatability of drag-force calibration for laminar-flow body.

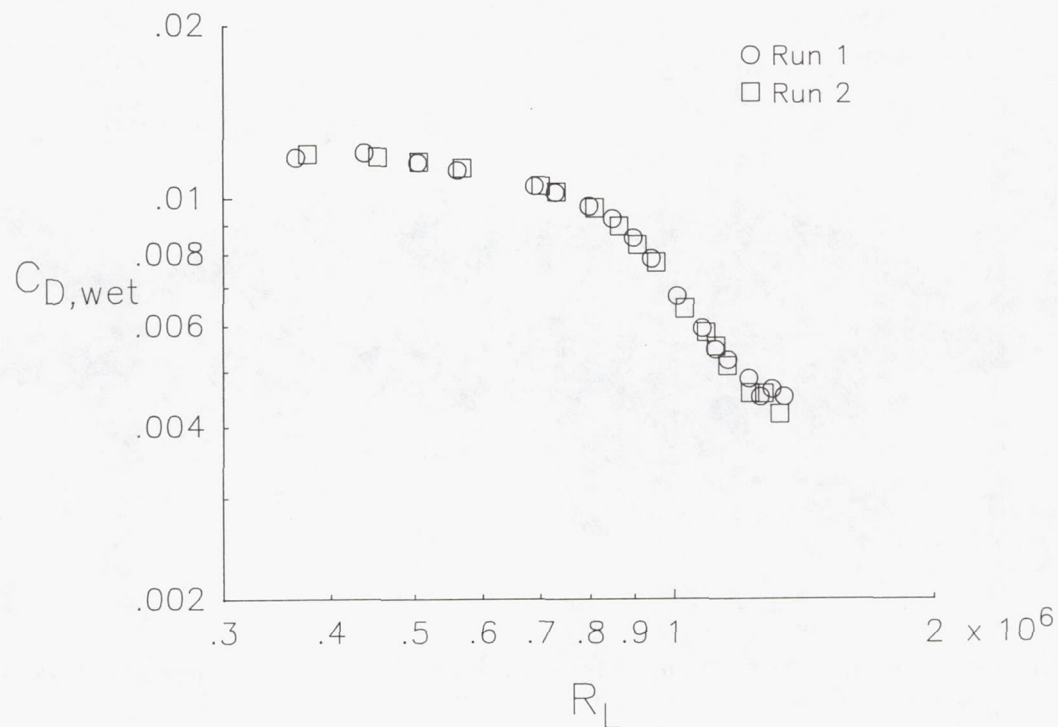


Figure 17. Drag characteristics of laminar-flow body.

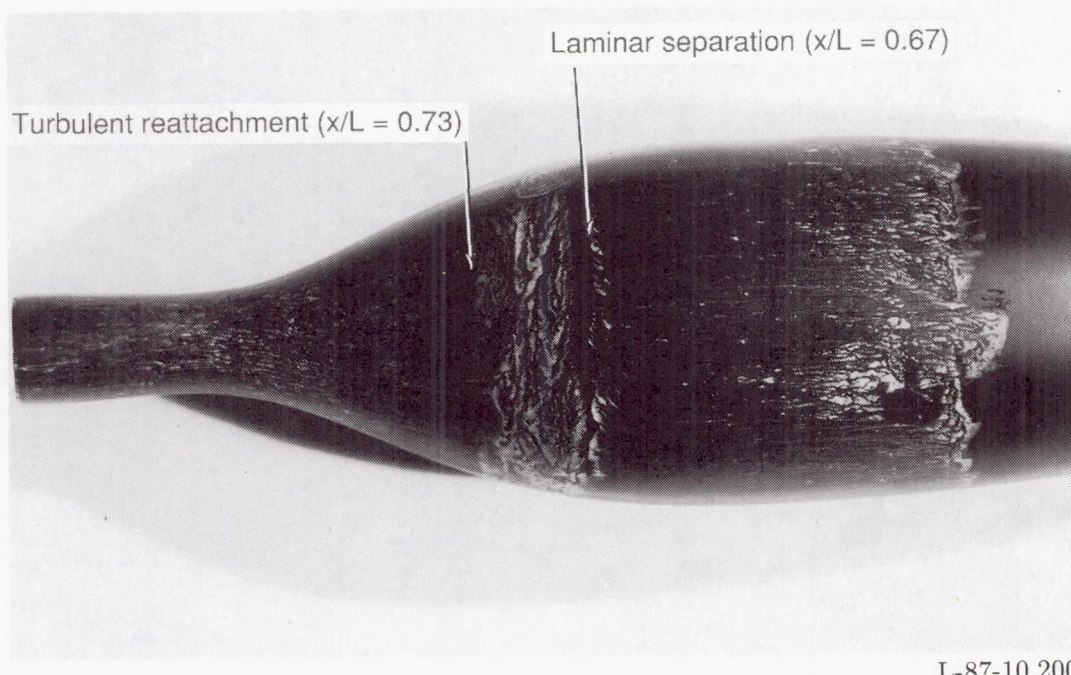
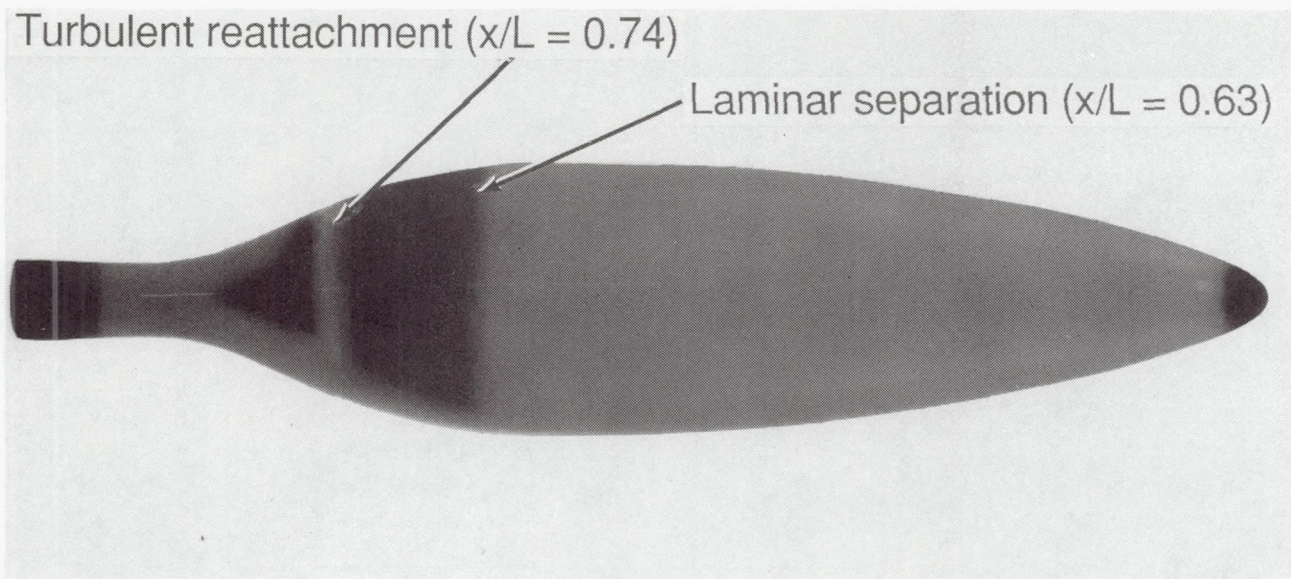


Figure 18. Oil flow visualization for free transition.  $R_L = 1.2 \times 10^6$ .



L-89-39

Figure 19. Liquid crystal flow visualization for free transition. Photograph artificially enhanced because of poor contrast on original negative.  $R_L = 1.2 \times 10^6$ .

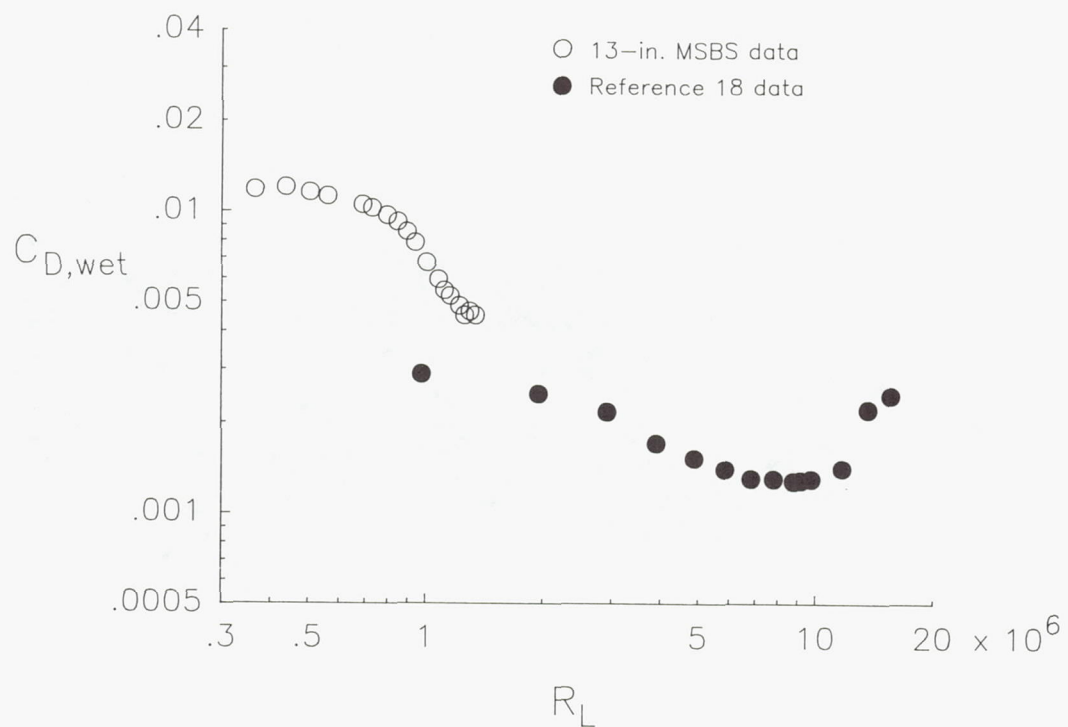


Figure 20. Measured drag characteristics and uncorrected data from reference 18.

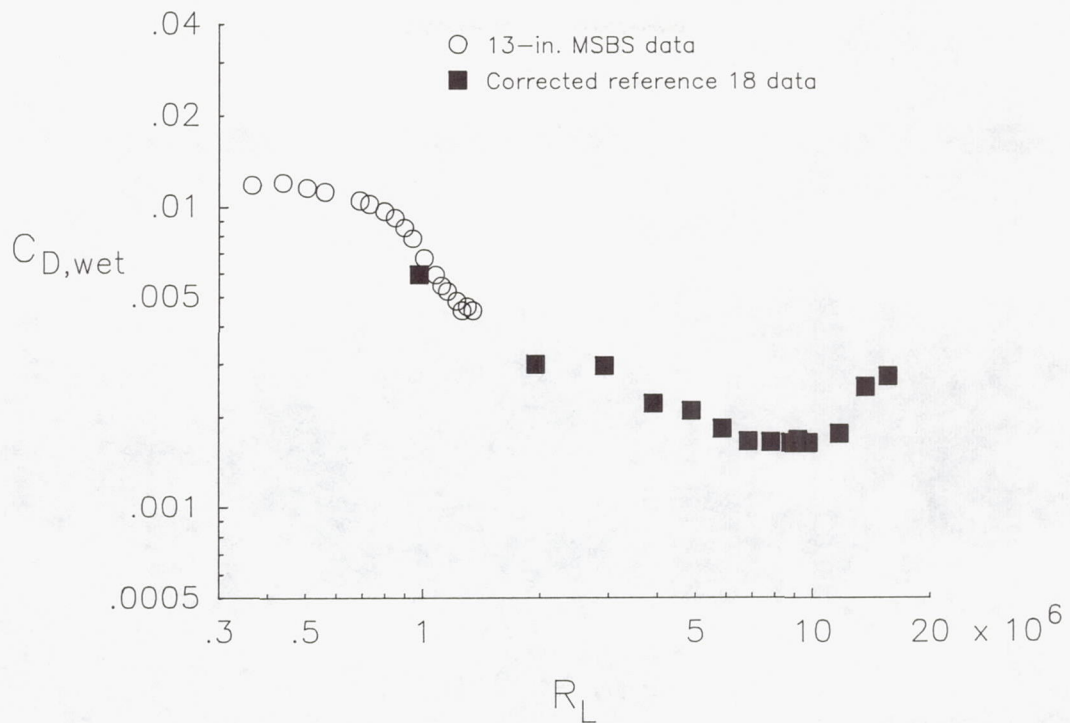


Figure 21. Measured drag characteristics and data from reference 18 corrected for cavity pressure.

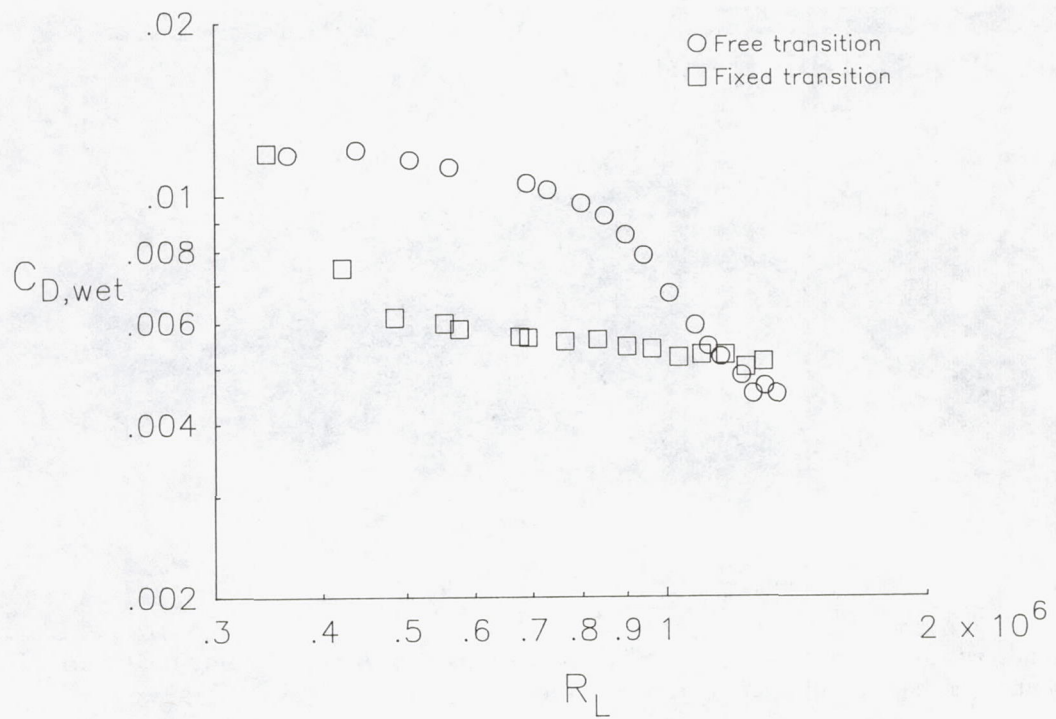
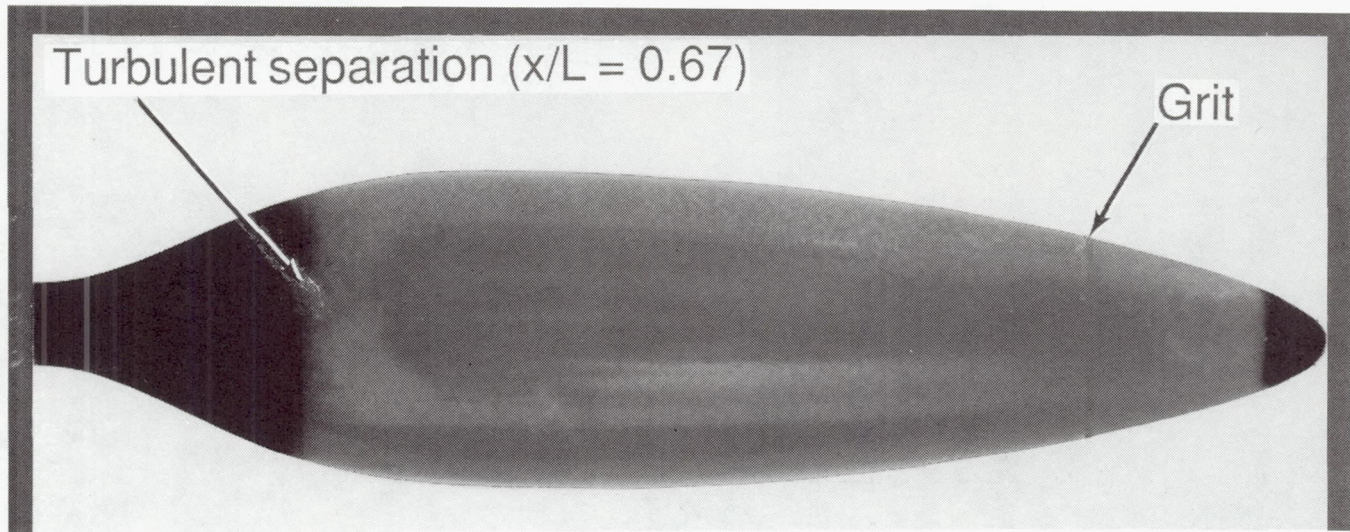
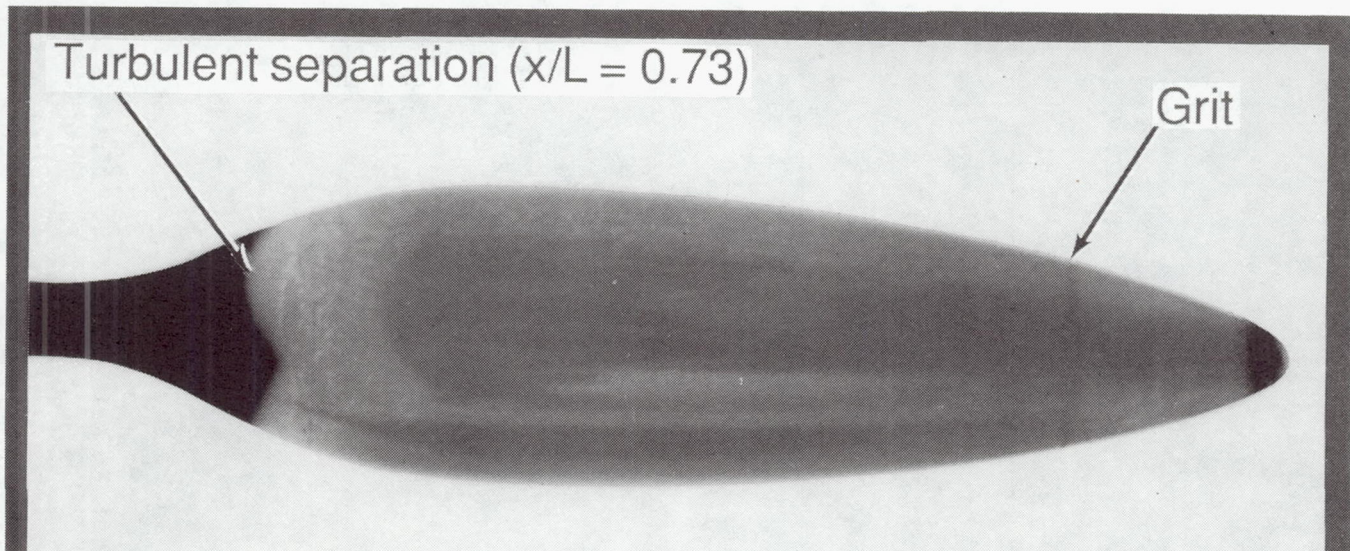


Figure 22. Drag characteristics of laminar-flow body with free transition and transition fixed at 17-percent station with no. 60 grit.



(a)  $R_L = 7.6 \times 10^5$ .



(b)  $R_L = 1.2 \times 10^6$ .

L-89-40

Figure 23. Liquid crystal flow visualization for fixed transition at  $x/L = 0.17$  using no. 60 grit. Photograph artificially enhanced because of poor contrast on original negative.

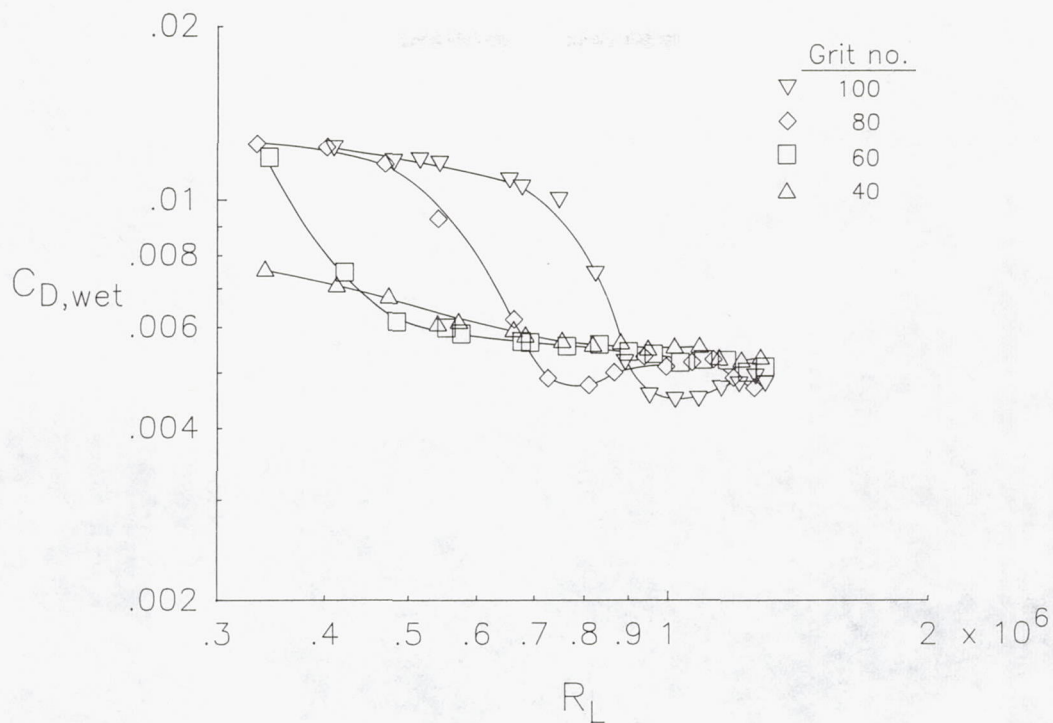


Figure 24. Drag characteristics of laminar-flow body with fixed transition at  $x/L = 0.17$  for four different grit sizes.

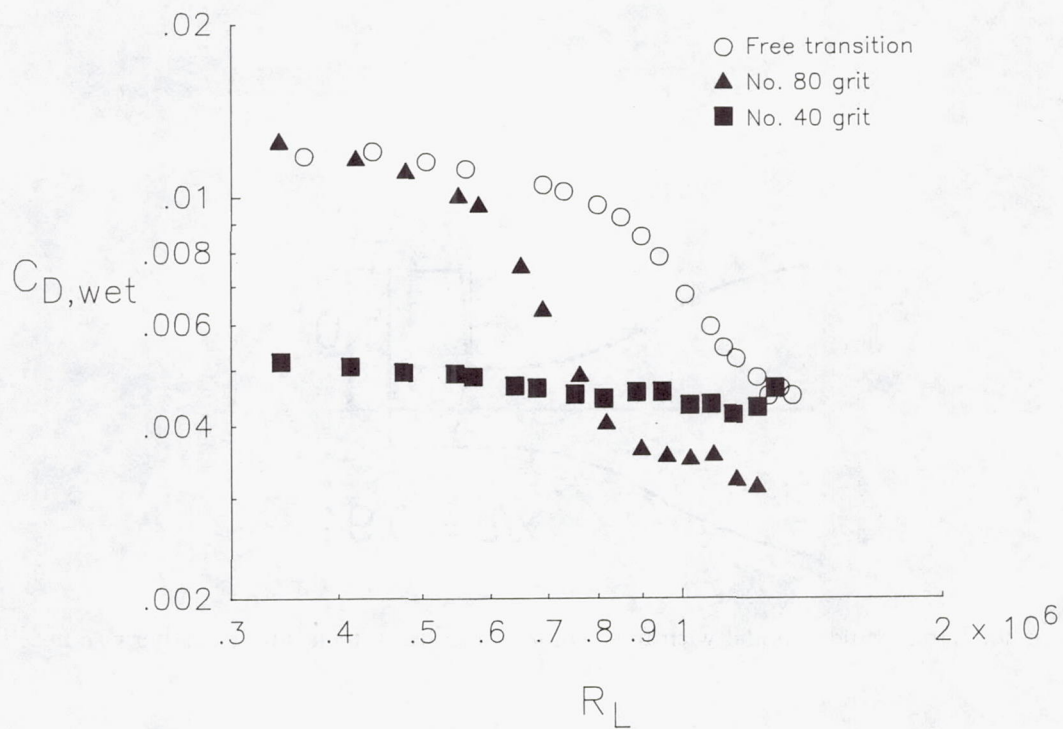
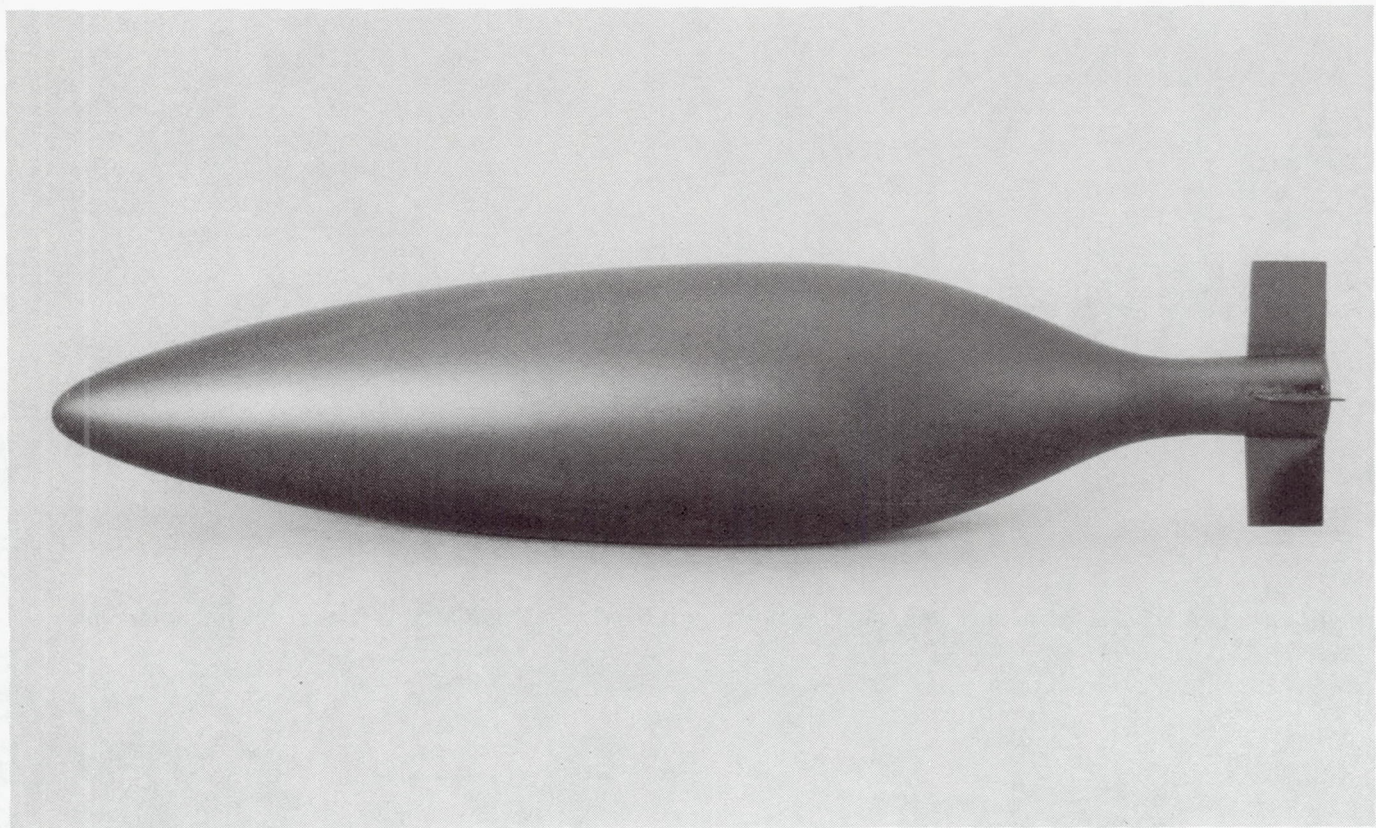


Figure 25. Drag characteristics of laminar-flow body with free transition and transition fixed at 50-percent station with both no. 80 and no. 40 grits.



L-87-11,135

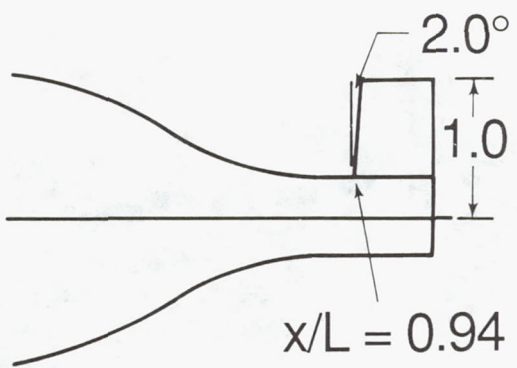


Figure 26. Laminar-flow model with fins. Dimensions are in inches unless otherwise noted.

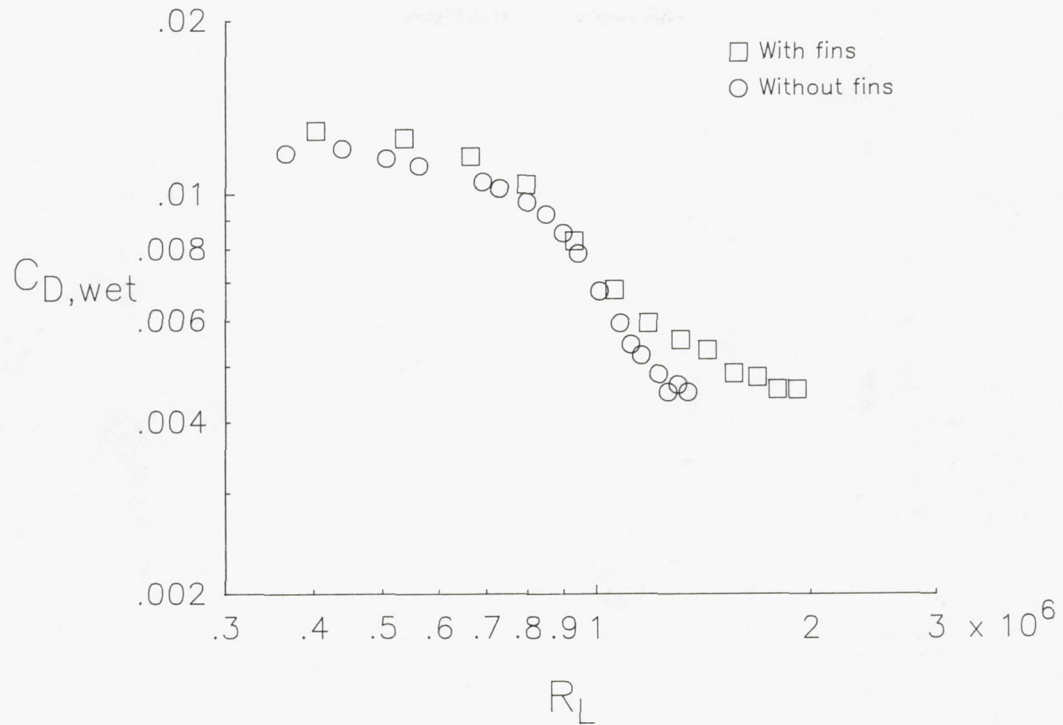


Figure 27. Drag characteristics of laminar-flow body with and without fins.

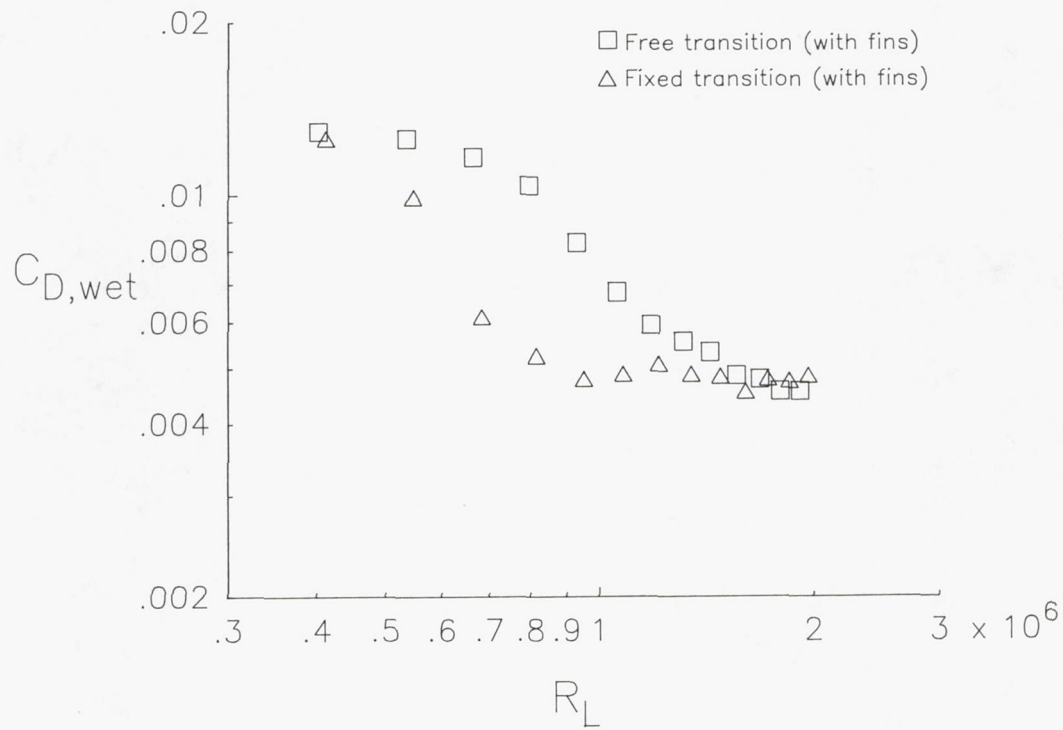


Figure 28. Drag characteristics of laminar-flow body with fins for free transition and transition fixed at  $x/L = 0.50$  with no. 80 grit.

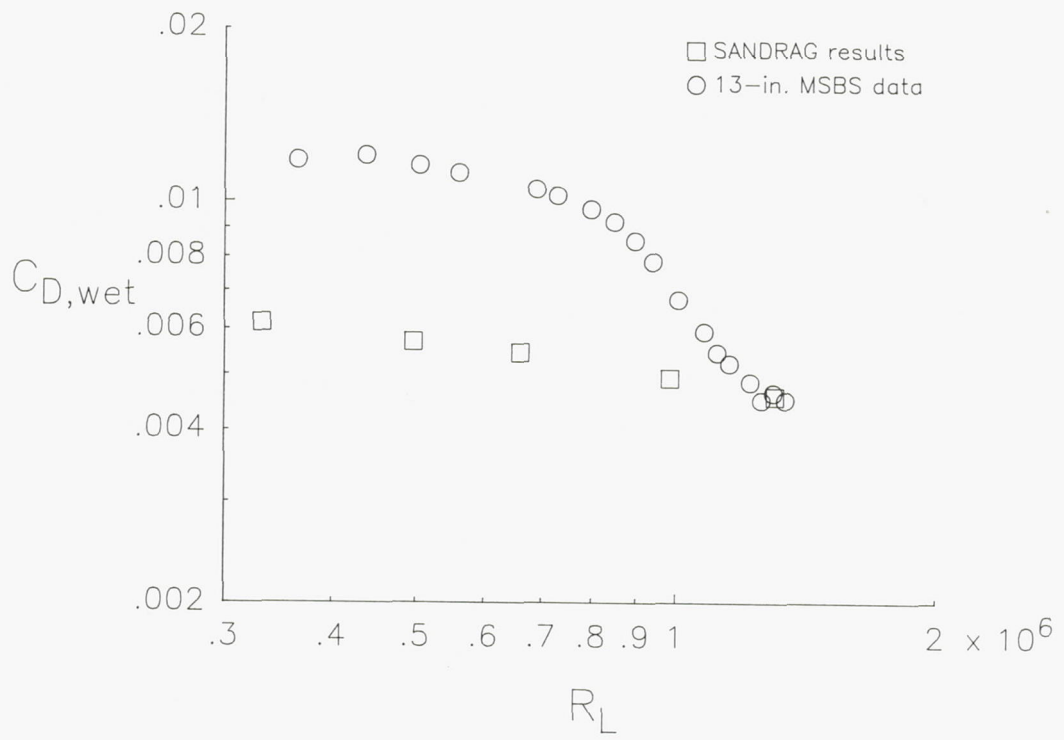


Figure 29. Drag characteristics of laminar-flow body computed with SANDRAG and measured during free transition.

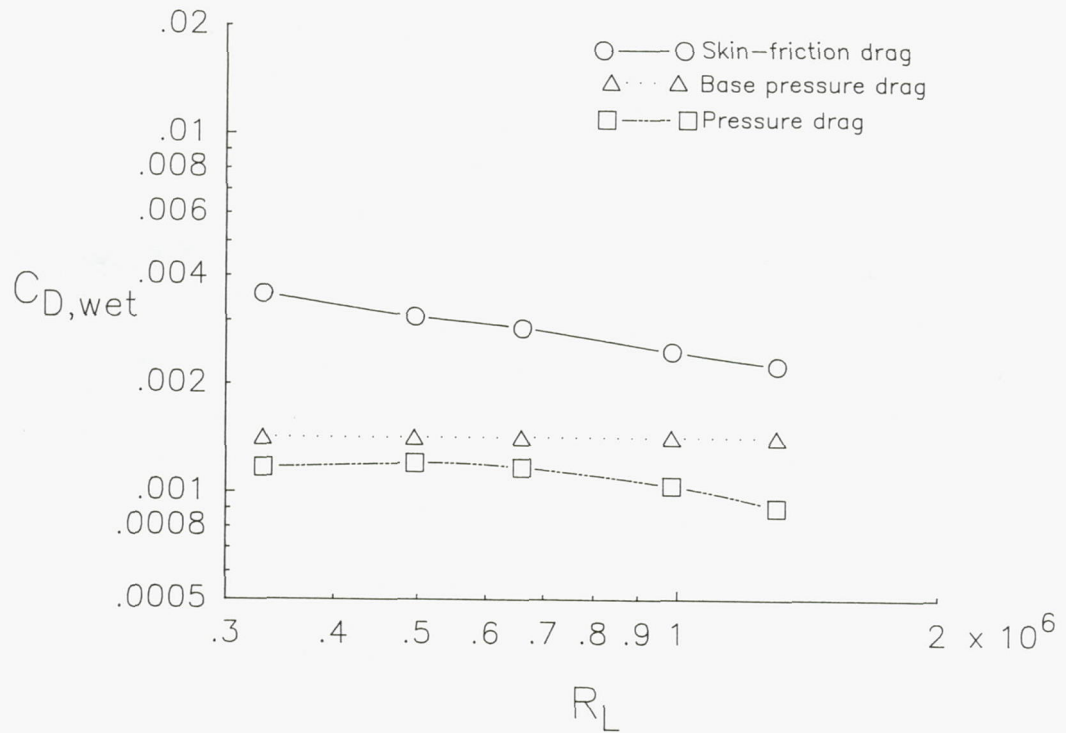


Figure 30. Breakdown of SANDRAG drag components.

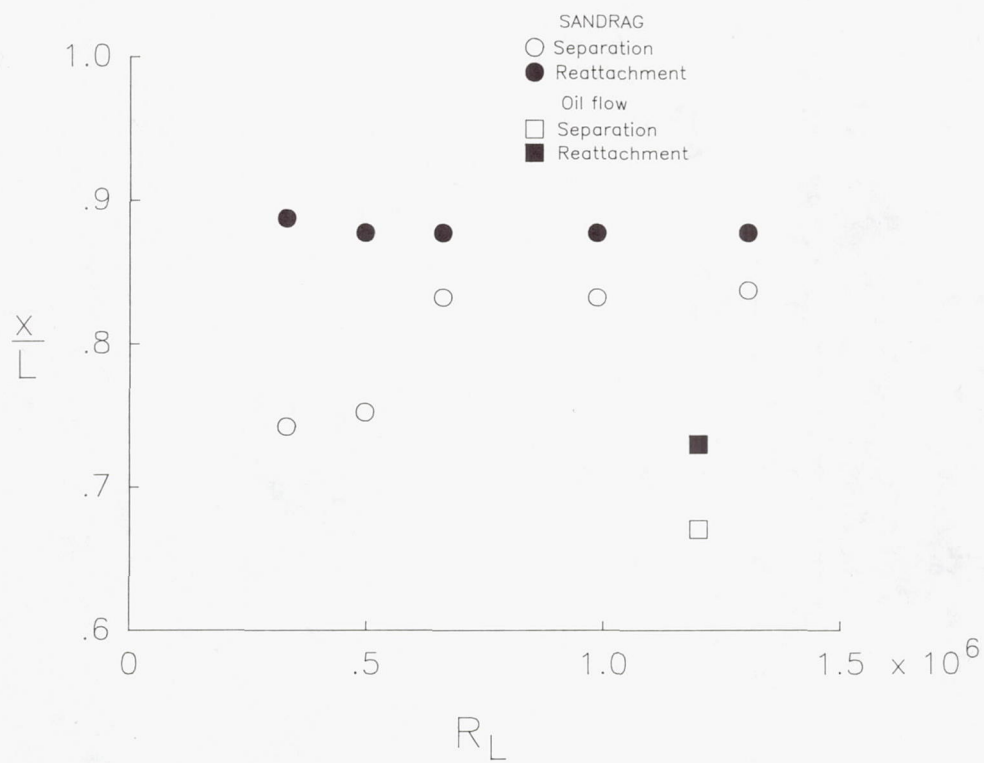


Figure 31. Separation and reattachment points from SANDRAG and from oil flow results.

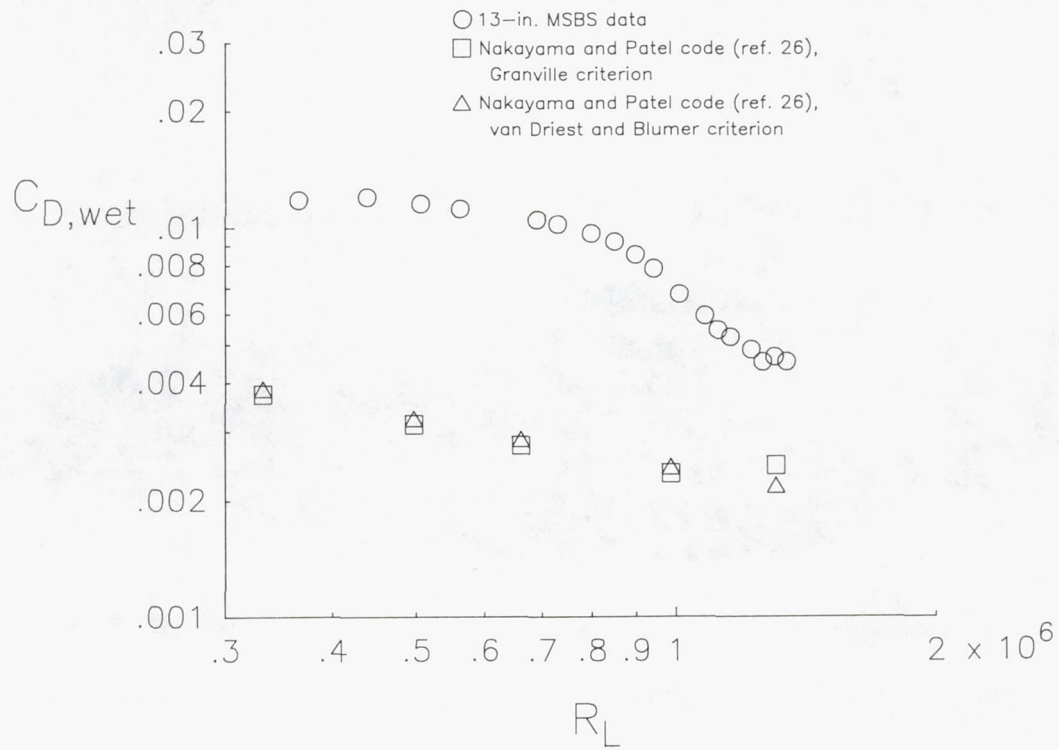


Figure 32. Drag characteristics of laminar-flow body computed with Nakayama and Patel code and measured during free transition.

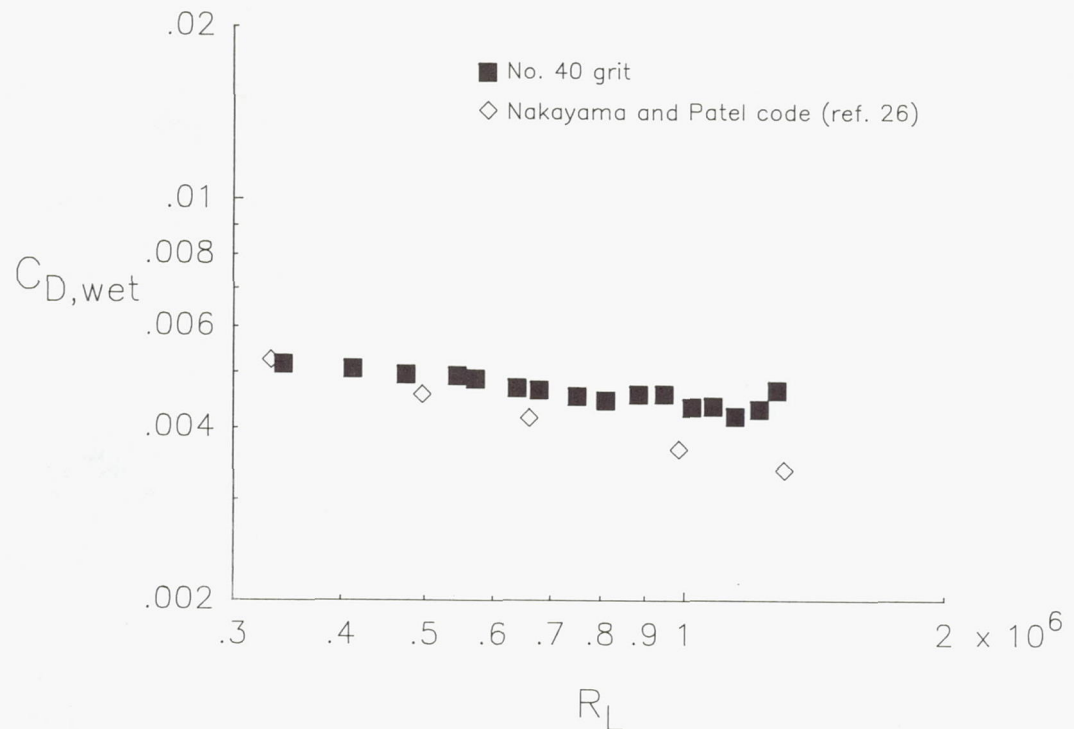


Figure 33. Drag characteristics of laminar-flow body computed with Nakayama and Patel code based on experimental transition location and measured for fixed transition at  $x/L = 0.50$  with no. 40 grit.

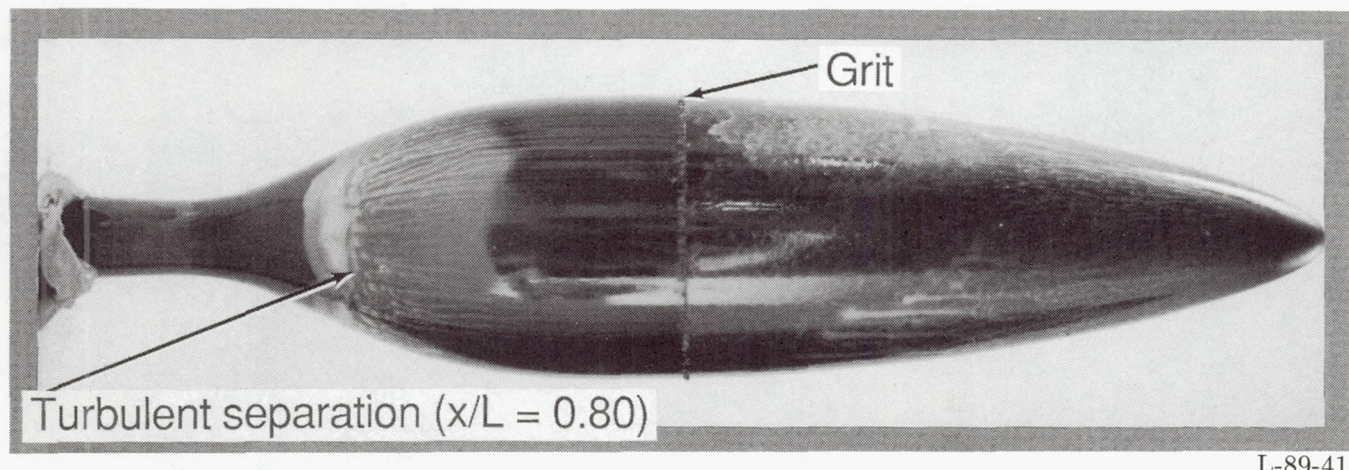


Figure 34. Liquid crystal flow visualization for transition fixed at  $x/L = 0.50$  with no. 40 grit.  $R_L = 1.1 \times 10^6$ .



## Report Documentation Page

1. Report No. NASA TP-2895	2. Government Accession No.	3. Recipient's Catalog No.	
4. Title and Subtitle Drag Measurements on a Laminar-Flow Body of Revolution in the 13-Inch Magnetic Suspension and Balance System		5. Report Date April 1989	
7. Author(s) David A. Dress		6. Performing Organization Code	
9. Performing Organization Name and Address NASA Langley Research Center Hampton, VA 23665-5225		8. Performing Organization Report No. L-16483	
12. Sponsoring Agency Name and Address National Aeronautics and Space Administration Washington, DC 20546-0001		10. Work Unit No. 505-61-01-02	
		11. Contract or Grant No.	
		13. Type of Report and Period Covered Technical Paper	
		14. Sponsoring Agency Code	
15. Supplementary Notes			
16. Abstract Wind tunnel measurements of drag force at low speeds were taken for a laminar-flow body of revolution free of support interference. This body was tested at zero incidence in the 13-inch Magnetic Suspension and Balance System (MSBS) at the Langley Research Center. The primary objective of these tests was to substantiate the capabilities of the MSBS for measuring drag force. The drag-force calibrations and wind-on repeatability data provided the means of assessing these capabilities. Additional investigations included (1) the effects of fixing transition, (2) the effects of fins installed in the tail, and (3) surface flow visualizations using both liquid crystals and oil flow. Also, two simple drag prediction codes were used to assess their usefulness in estimating overall body drag.			
17. Key Words (Suggested by Authors(s)) Magnetic suspension and balance system Body of revolution Drag measurements Laminar flow		18. Distribution Statement Unclassified—Unlimited	
Subject Category 02			
19. Security Classif. (of this report) Unclassified	20. Security Classif. (of this page) Unclassified	21. No. of Pages 35	22. Price A03